

Effects of finiteness on the thermo-fluid-dynamics of natural convection above horizontal plates

Abhijit Guha and Sayantan Sengupta

Citation: *Physics of Fluids* **28**, 063603 (2016); doi: 10.1063/1.4953382

View online: <http://dx.doi.org/10.1063/1.4953382>

View Table of Contents: <http://scitation.aip.org/content/aip/journal/pof2/28/6?ver=pdfcov>

Published by the **AIP Publishing**

Articles you may be interested in

[Computational study of flow-induced vibration of a reed in a channel and effect on convective heat transfer](#)

Phys. Fluids **26**, 127103 (2014); 10.1063/1.4903793

[Computational fluid dynamics analysis of a trapezoidal cavity absorber used for the linear Fresnel reflector solar concentrator system](#)

J. Renewable Sustainable Energy **4**, 063145 (2012); 10.1063/1.4772636

[Natural convection from inclined wall plumes in porous media](#)

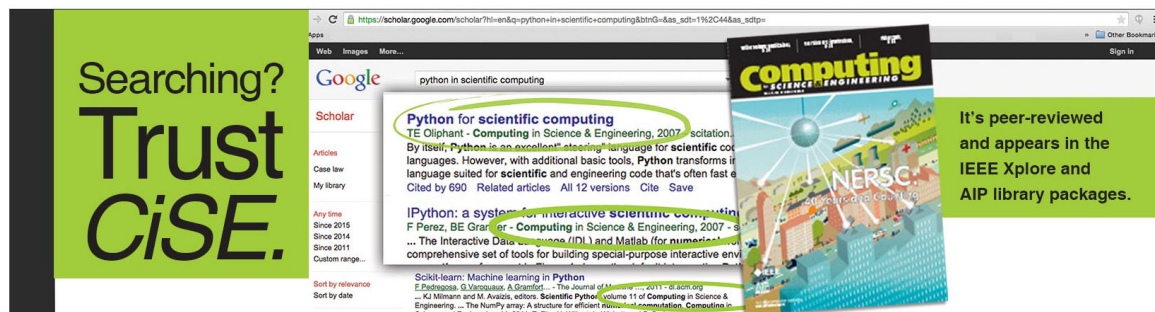
AIP Conf. Proc. **1453**, 179 (2012); 10.1063/1.4711172

[Natural convection in a bottom heated horizontal cylinder](#)

Phys. Fluids **17**, 064105 (2005); 10.1063/1.1932311

[Double diffusion natural convection in a rectangular enclosure filled with binary fluid saturated porous media: The effect of lateral aspect ratio](#)

Phys. Fluids **16**, 184 (2004); 10.1063/1.1630798



Searching? **Trust CiSE.**

Google Scholar search results for "python in scientific computing". The top result is "Python for scientific computing" by J. E. Oliphant, published in *Computing in Science & Engineering*, 2007. The snippet reads: "By itself, Python is an excellent modeling language for scientific computing languages. However, with additional basic tools, Python transforms into a language suited for scientific and engineering code that's often faster than C. Cited by 690. Related articles: All 12 versions. Cite. Save."

Other results include "IPython: a system for interactive scientific computing" by F. Perez, B. E. Granger, and "The Interactive Data Language (IDL) and Matlab for numerical computing: a comprehensive set of tools for building special-purpose interactive environments".

It's peer-reviewed and appears in the IEEE Xplore and AIP library packages.

Effects of finiteness on the thermo-fluid-dynamics of natural convection above horizontal plates

Abhijit Guha^{a)} and Sayantan Sengupta

*Mechanical Engineering Department, Indian Institute of Technology Kharagpur,
Kharagpur 721302, India*

(Received 28 February 2016; accepted 6 May 2016; published online 20 June 2016)

A rigorous and systematic computational and theoretical study, the first of its kind, for the laminar natural convective flow above rectangular horizontal surfaces of various aspect ratios ϕ (from 1 to ∞) is presented. Two-dimensional computational fluid dynamic (CFD) simulations (for $\phi \rightarrow \infty$) and three-dimensional CFD simulations (for $1 \leq \phi < \infty$) are performed to establish and elucidate the role of finiteness of the horizontal planform on the thermo-fluid-dynamics of natural convection. Great care is taken here to ensure grid independence and domain independence of the presented solutions. The results of the CFD simulations are compared with experimental data and similarity theory to understand how the existing simplified results fit, in the appropriate limiting cases, with the complex three-dimensional solutions revealed here. The present computational study establishes the region of a high-aspect-ratio planform over which the results of the similarity theory are approximately valid, the extent of this region depending on the Grashof number. There is, however, a region near the edge of the plate and another region near the centre of the plate (where a plume forms) in which the similarity theory results do not apply. The sizes of these non-compliance zones decrease as the Grashof number is increased. The present study also shows that the similarity velocity profile is not strictly obtained at any location over the plate because of the entrainment effect of the central plume. The 3-D CFD simulations of the present paper are coordinated to clearly reveal the separate and combined effects of three important aspects of finiteness: the presence of leading edges, the presence of planform centre, and the presence of physical corners in the planform. It is realised that the finiteness due to the presence of physical corners in the planform arises only for a finite value of ϕ in the case of 3-D CFD simulations (and not in 2-D CFD simulations or similarity theory). The presence of physical corners is related here to several significant aspects of the solution—the conversion of in-plane velocity to out-of-plane velocity near the diagonals, the star-like non-uniform distribution of surface heat flux on heated planforms, the three-dimensionality of the temperature field, and the complex spatial structure of the velocity iso-surfaces. A generic theoretical correlation for the Nusselt number is deduced for the averaged surface heat flux for various rectangular surfaces ($1 \leq \phi < \infty$) over a wide range of Grashof number. Innovative use of numerical visualization images is made to generate a comprehensive, quantitative understanding of the physical processes involved. *Published by AIP Publishing.* [<http://dx.doi.org/10.1063/1.4953382>]

I. INTRODUCTION

Natural convection above horizontal plates is such an important physical phenomenon that it is discussed routinely in most textbooks of heat transfer^{1,2} and fluid mechanics.^{3,4} This continues to be a vigorously active research area. A few examples of recent work on this topic can be found in Refs. 5–13. For laminar flow, theoretical treatments usually involve similarity theory or integral

^{a)} Author to whom correspondence should be addressed. Electronic mail: a.guha@mech.iitkgp.ernet.in

analysis assuming the surface to be semi-infinite; see Refs. 6 and 14–17. Although there exists a very limited number of experimental studies^{18–22} that explore the influence of size of the hot plate on the heat transfer rate, it is believed that the present work constitutes the first numerical study, involving extensive computational fluid dynamic (CFD) simulations, of the fundamentals of both fluid dynamics and heat transfer aspects of laminar natural convection as the finiteness of the heated surface is varied systematically. The results of the CFD simulations are compared with experimental data and similarity theory to understand how the existing simplified results fit, in the appropriate limiting cases, with the complex three-dimensional solutions revealed here.

The existence of natural convective flow above an upward facing heated (isothermal) horizontal flat plate was demonstrated mathematically by Stewartson.¹⁴ According to Stewartson, for horizontal orientation, the buoyancy has no component along the length of the plate. Thus, unlike a heated vertical plate where buoyancy causes natural convection directly, the natural convection above a heated horizontal plate evolves indirectly as buoyancy establishes an induced pressure gradient along the horizontal direction. A discussion on the physical mechanism responsible for such convection is given in Refs. 3 and 17 (Ref. 17 also provides a detailed discussion on the role of Prandtl number in natural convection, which is quite different from its well-known role in forced convection).

Stewartson¹⁴ considered a “semi-infinite” plate (a plate with only a single leading edge) and obtained a similarity solution. For a “semi-infinite” plate, there is no characteristic length scale. However, the present study focuses on finite plates. The effect of the physical dimensions of the plates results into complex thermo-fluid-dynamics which are very different from the predictions of the similarity theory. In the present paper, the effect of finiteness on the natural convective flow is studied with two related configurations which are heated isothermal lines and heated isothermal surfaces. For a heated isothermal line, boundary layer approximation (and consequently, similarity) does not hold near the centre and close to the leading edges. For a heated isothermal surface, boundary layer approximation (and consequently, similarity) does not hold near the centre, near the corners and close to the leading edges. The influences of these regions on the overall thermo-fluid-dynamics are demonstrated by solving full Navier-Stokes equations. In the case of heated isothermal lines, two-dimensional (2-D) CFD simulations are performed, and for heated isothermal surfaces, three-dimensional (3-D) CFD simulations are carried out. A connection between the results of 2-D simulations and the results of 3-D simulations is established in this paper.

A systematic method is employed for all CFD simulations. The actual quantitative dependence of the fluid dynamics and heat transfer on the input variables has been determined here through a comprehensive set of computations which involve a large number of separate computational fluid dynamic (CFD) simulations, each run to a high degree of convergence (the “scaled” residual for all conserved variables is set as 10^{-7} which is much smaller than what is normally set in much of the reported CFD work). Great care is taken here to ensure grid independence and domain independence (details given below) of the presented solutions. Moreover, second order accurate discretization schemes are used. This comprehensiveness and precision have helped us to formulate generic principles and identify subtle physical mechanisms.

Husar and Sparrow,²³ extending the method of Baker²⁴ for measurement of small fluid-velocity (0-5 cm/s), performed flow visualization studies for natural convective flow above upward facing heated planforms of various shapes (rectangular, square, circular, and triangular). They observed that a common characteristic of natural convective flows adjacent to planforms with corners is the partitioning of the flow field. They found that the partitions nearly superpose with the bisectors of the angles of the planform, and for a rectangular surface, the central partition is a longitudinal symmetry line. According to them, each partition line is a central element of a vertically ascending buoyant plume. Rotem and Claassen¹⁶ showed the existence of laminar boundary layers above heated horizontal surfaces by schlieren photographs. Goldstein and Lau²¹ carried out mass transfer experiments with approximately square naphthalene-plates in a sealed insulated room. Mass loss due to sublimation was measured by a remotely controlled balance, and temperature and atmospheric pressure were, respectively, measured by thermocouples and barometers from outside the test-room. According to them, their mass transfer experiment is analogous to a heat transfer experiment because in their experiment, the velocity of the fluid at the active surface is small. They concluded that despite the plume formation, the laminar boundary-layer flow seemed to exist near

the active surface. It is demonstrated here that the present CFD simulations (which are executed for rectangular and square planforms) are able to capture all of the above flow physics. Moreover, many other flow features which are difficult to realize from experimental observations are explored here. Some of these are mentioned below.

1. Two components of velocity, viz., in-plane and out-of-plane components, are calculated by CFD simulations. Transition from in-plane velocity to out-of-plane velocity near the partition lines is captured from the variation in shapes of the iso-surfaces of velocity components. In this context, some other flow features (e.g., the development of boundary layers, the interactions of the boundary layers, the zones of high and low in-plane velocity, and the zones of high and low out-of-plane velocity) are highlighted.
2. The effect of aspect ratio on the distributions of surface heat flux is demonstrated. The presence of physical corners and edge-effect is reflected in the distributions of surface heat flux.
3. Powerful numerical visualizations, obtained by post-processing of the CFD solutions, capture and present the quantitative details of the three-dimensionality of the velocity and temperature fields in relation to the geometric features of a finite planform; the completeness of this knowledge will be difficult to achieve through any other line of investigation—experimental or analytical.

In the past the problem of natural convection above horizontal plates was approached from various perspectives. This includes conceptualization of velocity and temperature fields by similarity theory, investigation of various flow physics above heated horizontal lines, and experimental identification of various regions above heated surfaces. One objective of the present work is to bring such different approaches under a common frame. The present solutions replicate the available results (or patterns) as well as create new quantitative understanding of the physical processes.

II. GOVERNING EQUATIONS

Navier-Stokes equations in the Cartesian coordinate system are the governing equations for natural convection above a heated horizontal plate. In this study, the flow is considered to be steady, laminar, and incompressible. The density is assumed to be constant except in the buoyancy terms (Boussinesq approximation). It is considered that other properties of fluid (dynamic viscosity μ , conductivity k , specific heat capacity c_p) vary negligibly. Viscous dissipation is also neglected (according to Gebhart,²⁵ the viscous dissipation term is important only when the induced kinetic energy becomes appreciable compared to the heat transfer). The conservation equations are as follows:

$$\frac{\partial u}{\partial x} + \frac{\partial v}{\partial y} + \frac{\partial w}{\partial z} = 0, \quad (1)$$

$$\rho_\infty \left(u \frac{\partial u}{\partial x} + v \frac{\partial u}{\partial y} + w \frac{\partial u}{\partial z} \right) = -\frac{\partial P}{\partial x} + \mu \nabla^2 u, \quad (2)$$

$$\rho_\infty \left(u \frac{\partial v}{\partial x} + v \frac{\partial v}{\partial y} + w \frac{\partial v}{\partial z} \right) = f_y - \frac{\partial P}{\partial y} + \mu \nabla^2 v, \quad (3)$$

$$\rho_\infty \left(u \frac{\partial w}{\partial x} + v \frac{\partial w}{\partial y} + w \frac{\partial w}{\partial z} \right) = -\frac{\partial P}{\partial z} + \mu \nabla^2 w, \quad (4)$$

$$\rho_\infty c_p \left(u \frac{\partial T}{\partial x} + v \frac{\partial T}{\partial y} + w \frac{\partial T}{\partial z} \right) = k \nabla^2 T. \quad (5)$$

The subscript ∞ indicates the ambient condition. In Equations (2)-(4), $P(\equiv p - p_\infty)$ is the gauge pressure. The body force f_y ($f_y = -\rho g$) is due to gravity. Gravitational acceleration is acting in the negative y -direction [i.e., inward normal to the heated horizontal surface which is placed on a (x, z) plane]. The density ρ in body force term is modelled according to Ref. 1,

$$\rho \approx \rho_\infty - \rho_\infty \beta (T - T_\infty), \quad (6)$$

where β is the coefficient of thermal expansion.

The coordinates x and y are non-dimensionalized by a reference length L^* . The non-dimensional coordinates are denoted as \bar{x} and \bar{y} . v/L^* is used as a reference velocity scale, and, \bar{u} , \bar{v} , and \bar{w} are the non-dimensional velocity components. The reference temperature scale is $(T_w - T_\infty)$ [T_w is the temperature of the isothermally heated surface]. The non-dimensional temperature is denoted by $\theta \equiv (T - T_\infty)/(T_w - T_\infty)$. Thus the non-dimensional governing equations are as follows:

$$\frac{\partial \bar{u}}{\partial \bar{x}} + \frac{\partial \bar{v}}{\partial \bar{y}} + \frac{\partial \bar{w}}{\partial \bar{z}} = 0, \quad (7)$$

$$\bar{u} \frac{\partial \bar{u}}{\partial \bar{x}} + \bar{v} \frac{\partial \bar{u}}{\partial \bar{y}} + \bar{w} \frac{\partial \bar{u}}{\partial \bar{z}} = -\frac{\partial \bar{P}}{\partial \bar{x}} + \nabla^2 \bar{u}, \quad (8)$$

$$\bar{u} \frac{\partial \bar{v}}{\partial \bar{x}} + \bar{v} \frac{\partial \bar{v}}{\partial \bar{y}} + \bar{w} \frac{\partial \bar{v}}{\partial \bar{z}} = -\frac{\partial}{\partial \bar{y}} \left(\bar{P} + \frac{gL^{*3}\bar{y}}{\nu^2} \right) + \nabla^2 \bar{v} + Gr \theta, \quad (9)$$

$$\bar{u} \frac{\partial \bar{w}}{\partial \bar{x}} + \bar{v} \frac{\partial \bar{w}}{\partial \bar{y}} + \bar{w} \frac{\partial \bar{w}}{\partial \bar{z}} = -\frac{\partial \bar{P}}{\partial \bar{z}} + \nabla^2 \bar{w}, \quad (10)$$

$$\bar{u} \frac{\partial \theta}{\partial \bar{x}} + \bar{v} \frac{\partial \theta}{\partial \bar{y}} + \bar{w} \frac{\partial \theta}{\partial \bar{z}} = \frac{1}{Pr} \nabla^2 \theta. \quad (11)$$

In Equations (8)-(10), \bar{P} equals $PL^{*2}/(\rho_\infty \nu^2)$. The procedure for obtaining the non-dimensional Equations (7)-(11) is adopted from Ref. 16.

The above set of equations contains two non-dimensional numbers, viz. Grashof number (Gr) and Prandtl number (Pr). Gr and Pr are expressed as follows:

$$Gr = \frac{g\beta(L^*)^3(T_w - T_\infty)}{\nu^2} \quad (12)$$

and

$$Pr = \frac{\mu c_p}{k}. \quad (13)$$

Grashof number is interpreted as a ratio of the buoyancy to viscous forces, and the Prandtl number is usually defined as a ratio of the momentum to thermal diffusivities,²⁶ but please see Ref. 17 for a detailed discussion on the role of Prandtl number in natural convection.

III. METHOD OF SOLUTION

In this paper, the set of Equations (1)-(5) is solved to resolve the three-dimensional flow-field above an isothermally heated horizontal plate. It is mentioned in Sec. II that this heated surface of the plate is a (x, z) plane. Let us consider that ΔL_x and ΔL_z are the extents of the surface, respectively, along x -direction and along z -direction. If ΔL_x is of the order of ΔL_z then full three-dimensional simulations are required to analyse fluid flow and heat transfer. On the other hand, if ΔL_z is sufficiently greater than ΔL_x then, in most of the region (excluding regions near two ends of the plate), the contribution of the terms associated with velocity component w [in Equations (1)-(5)] will be weak. And, a reduced set of equations, which is obtained by substituting $w = 0$ in Equations (1)-(5), will be sufficient to predict the flow physics in most regions of the plate. Two-dimensional simulation is performed to obtain such flow field.

In the present paper, the flow is considered to be laminar. The natural convective flow above a heated surface may, however, become unstable above a critical Gr . Pr . Rotem and Claassen,¹⁶ in their experiments, observed that for a fixed Pr , the increase in Gr results into a thickening of boundary layer. According to them, for a large Gr , the flow attains a point of instability well before arriving near the axis of symmetry. They describe two possible modes of instability. In the first mode, a separation of a thick, slow boundary layer occurs due to the insufficiency of the pressure gradient to drive the flow (gravitational instability). A nonlinear interaction between mutually perpendicular pressure gradient and destabilizing buoyancy force is involved in this instability. In the other mode, with an increase in Gr , the width of the zone, over which the laminar boundary-layer exists, will decrease. The critical Gr corresponding to the second mode is less than that corresponding to the

first mode. To the best of our knowledge, Rotem and Claassen commented only on the normal and the lateral extents of the laminar layers. According to Goldstein and Lau,²¹ the three-dimensional effect on a finite plate may lower the critical Gr further. Kitamura and Kimura²² performed a detailed experiment and provided a more detailed discussion on this three-dimensional effect. The criterion for critical Gr . Pr set in the present study is adopted from the experimental study of Lloyd and Moran.¹⁹ By conducting experiment on various shaped (right-triangular, rectangular, square and circular) finite horizontal surfaces, Lloyd and Moran¹⁹ concluded that the transition from laminar to turbulent flow takes place at about Gr . $Pr = 8 \times 10^6$ (the reference length scale used by them is the ratio of surface area to surface perimeter). The critical Gr . Pr given in Ref. 19 is close to the critical Gr . Pr obtained by Al-Arabi and El-Riedy.²⁰ Other than keeping Gr . Pr less than the critical value, we have taken care of preserving another condition. This condition is related to the height of the rising plume above the heated surface. Due to entrainment, the local Reynolds number of the plume increases with an increase in the vertical distance from the heated surface. According to Dimotakis,²⁷ for fully developed turbulent flow, the value of local Reynolds number Re_y ($Re_y \equiv v\delta/\nu$) should exceed 10^4 (δ is the local width of a jet at any y). For the present simulations, Re_y is kept well below this value.

Both two-dimensional (2-D) and three-dimensional (3-D) simulations are carried out by a commercially available CFD software Fluent 6.3.26.²⁸ Double precision, pressure based, steady and implicit solver is used. The SIMPLE algorithm, with second order upwind scheme for momentum and energy equations and second order pressure-discretization, is utilized. Under-relaxation factors for momentum, energy, pressure, density, and body force are chosen, respectively, 0.7, 1, 0.3, 1, and 1. A systematic procedure, which includes many precautions and care, is employed for both 2-D and 3-D simulations. The procedure, with an example 2-D simulation, is described below in Sections III A–III E. The techniques followed for 3-D simulations are similar, and therefore, only a brief description is given in Section III F.

A. Physical configuration and boundary conditions

Figure 1 shows the schematic diagram of the physical configuration. The top surface of the plate is heated and an isothermal condition ($T = T_w$) is maintained. All other surfaces of the plate are insulated. The full domain ABB^*A^* is symmetric about DC. Hence, ABCD is considered as the computational domain. The x -coordinate is along the length of the plate; and y -coordinate is normal to the surface of the plate (the z -coordinate, which is not relevant for 2-D simulations, is perpendicular to the plane of the paper). The point of intersection between DC and the isothermal surface is the origin (o) of the coordinate system (2-D Cartesian).

The geometry of the plate, boundary conditions and working fluid are provided in Table I. For this case, the reference length scale is equal to the half of the plate-length; it is denoted by L ($L = \Delta L_x/2$). No slip boundary condition is set on all the surfaces (isothermal and insulated surfaces) of the plate. The boundaries DA, AB, and BC are modelled by the “pressure outlet” option offered by Fluent,²⁸ with zero gauge pressure. “Symmetry” is applied on DC. Air is used as working fluid. Necessary dimensional values corresponding to the representative 2-D simulation (which is used to describe all the tests given in Sections III A–III E) are also mentioned in Table I. The values of Gr and Pr are taken as 2×10^6 and 0.7068, respectively.

B. Domain independence test

It is shown in Figure 1 that the plate is surrounded by a dotted line which is the region of interest (ROI). The boundary of the ROI is closer to the plate as compared to the boundary of ABB^*A^* . From the hot surface, l_t , l_b , and l_s are the respective distances of the top boundary, bottom boundary, and side boundary of the ROI (see Figure 1). The solution within ROI should be independent of the size of the computational domain. This is achieved when the size of the domain is adequately large. Such a domain is obtained through a domain independence test.

Table II shows five representative 2-D computational domains (D1, D2, D3, D4, and D5) for which the results of the domain independence test are presented here. The respective sizes of the five domains are mentioned in Table II. D1 is the smallest and D5 is the largest domain. For the

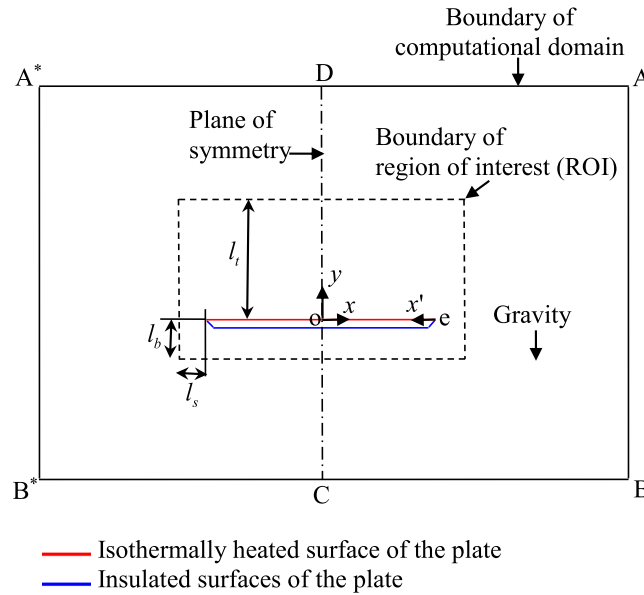


FIG. 1. Schematic diagram of the physical configuration.

geometry and other details given in Table I, 2-D simulations are performed separately for each domain. For all domains, the non-dimensional velocity components are calculated on top, bottom, and side boundaries of the ROI. Figure 2 shows the computed values of \bar{u} on the side boundary and the computed values of \bar{v} on top and bottom boundaries of the ROI (all boundaries of the ROI considered in Figure 2 are located at the right side of the symmetry plane DC). Figure 2 demonstrates that any further enlargement beyond the size of D4 will produce negligible change of the solutions within the ROI. Hence, according to the domain independence test, D4 is an appropriate domain corresponding to the geometry and operating conditions given in Table I.

C. Grid independence test

Table III shows a few pertinent details corresponding to a grid independence test that is carried out for the representative 2-D simulation (details given in Table I). Based on this study, a total 63 200 mapped, quadrilateral computational cells are selected for this 2-D simulation. The grids are distributed in the x and y directions in accordance with the difference in the flow physics in the two directions. The grid distribution in the y -direction is non-uniform with very small grid size close to the surfaces of the plate (to capture the velocity gradient on the surface accurately) and with progressively larger grid size towards the boundary of the computational domain. The grid distribution in the x -direction is also non-uniform. The size of the grids is very small close to the

TABLE I. Geometry, boundary conditions and working fluid used in the example 2-D simulation.

Geometry	Boundary conditions	Fluid	Dimensional values
<i>Plate geometry</i> : Half of the plate length = L (i.e., oe in Figure 1) Plate-thickness = $0.02L$	Upper surface of the plate	No slip, isothermal ($T = T_w$)	Air $L = 0.1$ m; $p_\infty = 101\,325$ Pa; $T_w = 315.5$ K; $T_\infty = 300$ K
	Lower surfaces of the plate	No slip, insulated ($q_w = 0$)	
<i>Geometry of the "region of interest"</i> : $l_t = L$; $l_b = L/4$; $l_s = L/4$	CD in Figure 1	Symmetry	
	DA, AB, and BC in Figure 1	Pressure outlet	

TABLE II. Five representative (two-dimensional) computational domains for which the results of the domain independence test is presented here.

Name of the computational domain	Non-dimensional distances (all distances are non-dimensionalized by L)		
	Above l_t	Below l_b	Beyond l_s
D1	0.5	0.75	0.75
D2	1	1.25	1.25
D3	1.5	1.75	1.75
D4	2	2.25	2.25
D5	2.25	2.75	2.75

edge of the plate. The size of the grids increases progressively towards the plane of symmetry (DC) and towards the boundary AB.

Table III shows the computed values of the averaged Nusselt number Nu_L ($Nu_L \equiv h_{avg}L/k$) for three different grid distributions (coarse, standard, and fine). While increasing the number of cells simultaneously in the x and y directions, it is found that the computed value of Nu_L varies until the “standard” grid distribution (corresponding to a total of 63 200 computational cells) is attained. Any further increase of cells leads to a marginal change of Nu_L (compare “standard” and “fine” grid distributions). Additionally, the local variations of velocity and temperature within the ROI are examined for these three different grid distributions. “Standard” grid distribution is thus selected through such investigations.

D. Selection of convergence criterion

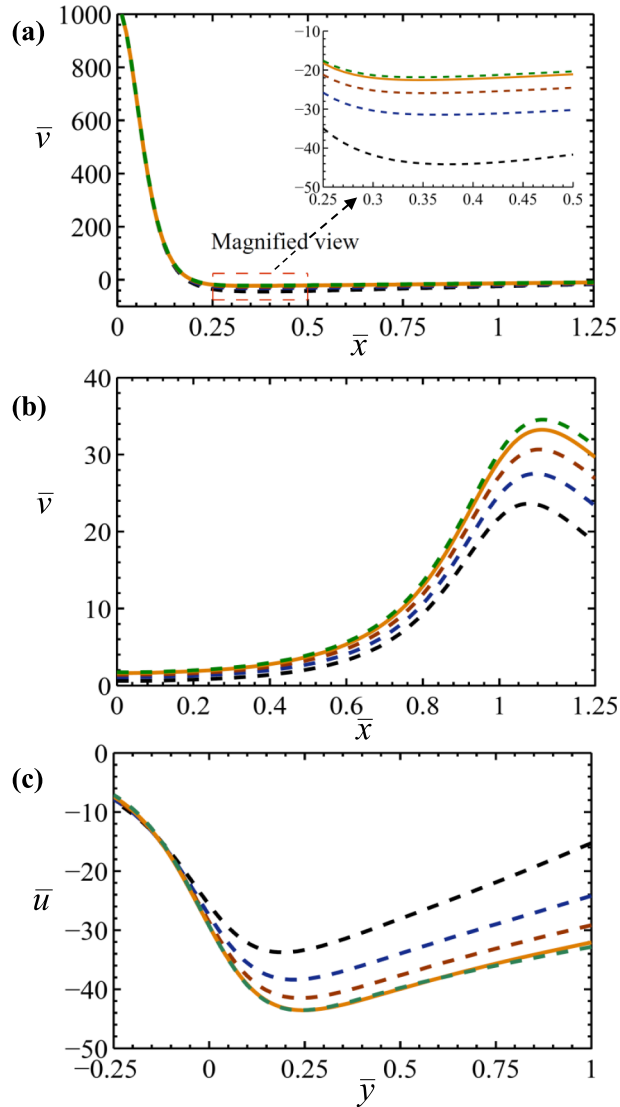
A systematic method is employed to select an appropriate convergence criterion. For this, CFD iterations with a given geometry and boundary conditions (see Table I) are progressed up to three different levels of convergence; in each run the maximum “scaled” residual²⁸ for all conserved variables (i.e., mass, velocity components, and energy) is set at a particular value, the three values used in the three runs being 10^{-6} , 10^{-7} , and 10^{-8} . It is found that when the maximum “scaled” residual is changed from 10^{-7} to 10^{-8} , the corresponding change in Nu_L is less than 0.0036%. Hence, a maximum “scaled” residual of 10^{-7} is chosen as the convergence criterion for the present study.

E. Effect of varying edge geometry

It is already mentioned in Section III C that near the edge of the plate, the solution is sensitive to the size of the grid, and a very small grid is required to capture the flow physics properly. The planes, which define the thickness of the plate, may be straight or chamfered (inclined). It is interesting to examine the near edge (fluid dynamic) details of a straight edge plate and that of a chamfered edge plate (see Figure 3). Figures 3(a) and 3(b) show the contours of non-dimensional velocity magnitude ($\sqrt{u^2 + v^2}L/\nu$), respectively, for a chamfered edge plate and for a straight edge plate. Figure 3(c) shows the y -variation of \bar{u} at the leading edges of both plates. There is a little difference between the two solutions, particularly in the peak velocity, at the leading edge of the plates as can be seen in Figures 3(a)–3(c). However, no striking difference is observed overall. The other issue, which is resolved in this subsection, is the effect of varying plate-thickness. It is observed that when the plate-thickness varies from $0.02L$ to $0.01L$, the y -profile of \bar{u} at the leading edge of the plate changes negligibly (see Figure 3(c)). The objective of these two separate tests is to examine the sensitivity of the computational fluid dynamic (CFD) solutions on these two issues (viz., varying shape and varying thickness of the plate-edge).

F. A brief description of the 3-D CFD method

The 2-D simulations are executed on a (x , y) plane. In 3-D simulations, the z -extent of the finite plate has also been considered. To reduce the computational time, the 3-D simulations are



Keys used to represent the five domains described in Table 2:
 ----- D1; ---- D2; - - - - D3; ——— D4; - - - - D5.

FIG. 2. Results of 2-D CFD simulations for domain independence test: (a) top boundary of ROI; (b) bottom boundary of ROI; (c) side boundary of ROI (all results correspond to $Gr = 2 \times 10^6$ and $Pr = 0.7068$).

carried out in a reduced domain which is one fourth of the full computational domain. A similar technique was adopted in the case of 2-D simulations. Figure 1 shows that, utilizing a symmetry plane, only half of the full domain is used for 2-D computations. In the case of 3-D simulations, two mutually perpendicular symmetry planes, passing through the origin, are considered to extract one

TABLE III. Grid independence test (the representative results correspond to the geometry, boundary conditions, and working fluid given in Table I).

Grid distribution for 2-D CFD simulations	Total number of cells	Nu_L
Coarse	30 825	10.80
Standard	63 200	10.86
Fine	130 200	10.85

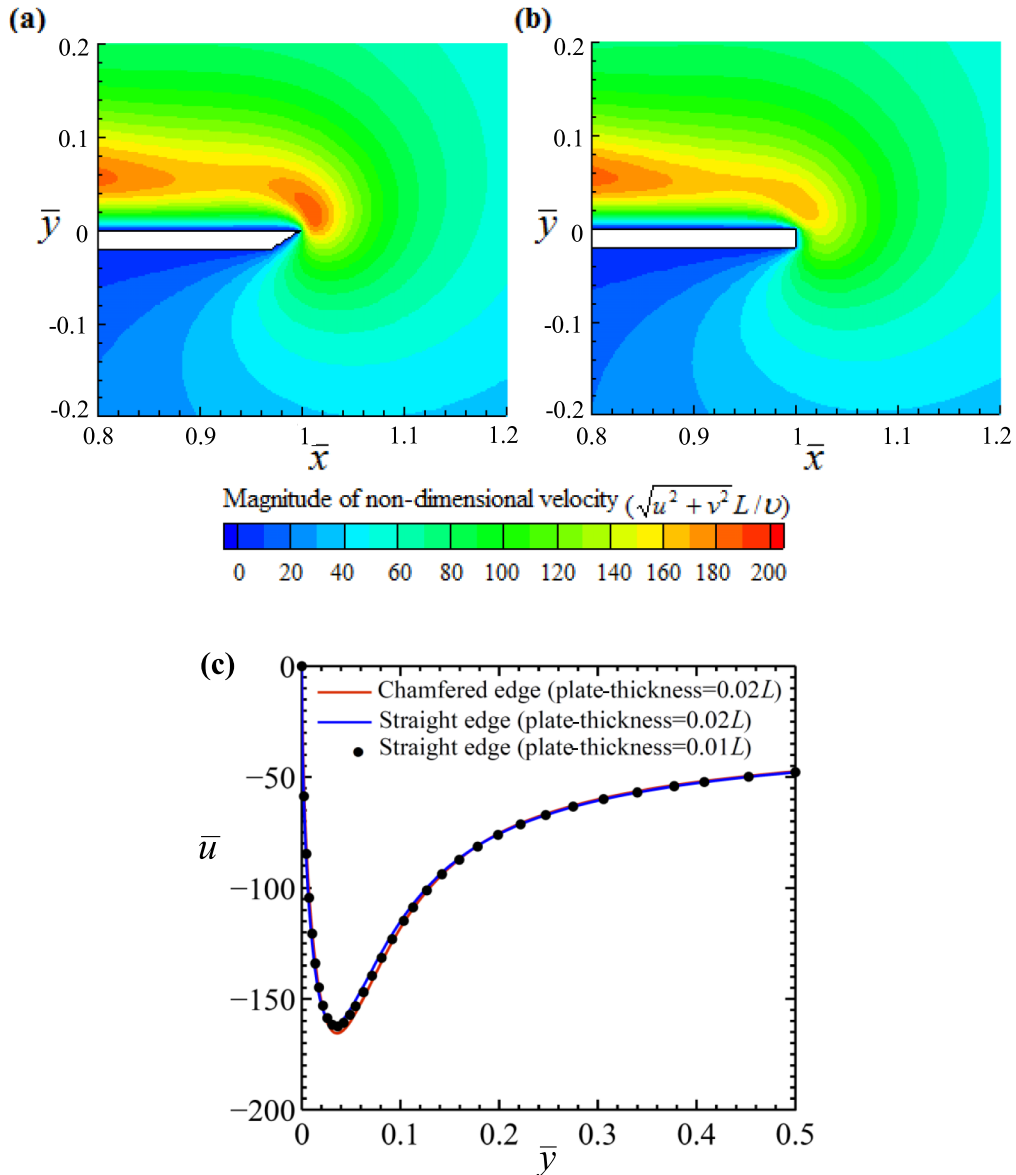


FIG. 3. Prediction of 2-D CFD simulations for varying edge geometry: (a) velocity-contours for a chamfered edge plate; (b) velocity-contours for a straight edge plate; (c) \bar{u} versus \bar{y} profiles at the edge of the plate ($\bar{x} = 1$) for various edge geometries and plate-thicknesses (all results correspond to $Gr = 2 \times 10^6$ and $Pr = 0.7068$).

fourth of the full domain. One of the two symmetry planes is a (y, z) plane, while the other is a (x, y) plane.

No slip is applied on all surfaces of the plate. Isothermal condition is specified at the top surface of the plate and other surfaces of the plate are insulated. The locations of the planes, where the pressure outlet boundary conditions are set, are determined through a domain independence test, as described in Section III B. A maximum “scaled” residual of 10^{-7} is chosen as the convergence criterion (Section III D). The grid distributions in x , y , and z directions are selected through a grid independence test (Section III C).

For brevity, we describe here only a sample case of the 3-D grid independence test. An isothermal ($T_w = 315.5$ K) square plate (each side of the square equals 0.2 m, i.e., $L = 0.1$ m) is considered. All other details required for the 3-D simulations (plate thickness, working fluid, p_∞ and T_∞) are the same as given in Table I. The adopted region of interest (ROI) is a 3-D space; if one

considers a z -extent of the sketch given in Figure 1, then there would be two values of the parameter l_s - one in the x -direction and the other in the z -direction. A systematic 3-D domain independence test, similar to what is described in Section III B, is conducted to obtain the following values of the required geometric parameters of ROI: $l_t = L$, $l_b = L/4$, and $l_{s,x \text{ direction}} = l_{s,z \text{ direction}} = L/4$.

For the 3-D grid independence test for the sample case described above, a coarse mesh containing 496 500 cells, the standard mesh of 1 352 025 cells, and a fine mesh of 3 116 350 cells are used. Simulations carried on these three meshes gave the following values of the Nusselt number: $Nu = 13.71$ for the coarse mesh, $Nu = 13.67$ for the standard and $Nu = 13.68$ for the fine mesh. A study of these values of Nu justifies why the standard mesh is adopted for further numerical computations for this plate geometry. Similar grid independence test was carried out for each of the other square and rectangular plate geometries for which results are presented in this paper.

IV. RESULTS OF 2-D CFD SIMULATIONS

In this section, the results of the present 2-D CFD simulations are presented. Velocity and temperature distributions above heated isothermal lines are described in Section IV A. A comparison of the results of the 2-D simulations with the predictions of the similarity theory is given in Section IV B.

A. Velocity and temperature distributions

Figures 4(a) and 4(b) show the contours of non-dimensional velocity magnitude and the contours of non-dimensional temperature, respectively. The figure displays both sides of the plane of symmetry for the ease of readers' understanding. The geometry and boundary conditions for the simulation are the same as given in Table I ($Gr = 2 \times 10^6$ and $Pr = 0.7068$). Some interesting fluid dynamic features extracted from Figures 4(a) and 4(b) are given below.

Near the plane of symmetry, a plume is formed. The magnitude of velocity inside the plume is large as compared to the other regions of the domain. It can be shown that the direction of velocity within the plume is almost normal to the hot surface, and v is the major component. The plume-width broadens slowly after a certain vertical distance from the heated surface (Figure 4(a)). This occurs due to the horizontal diffusion which introduces a non-zero u velocity required for the entrainment within a buoyant plume. Within the plume, the variation of temperature in the

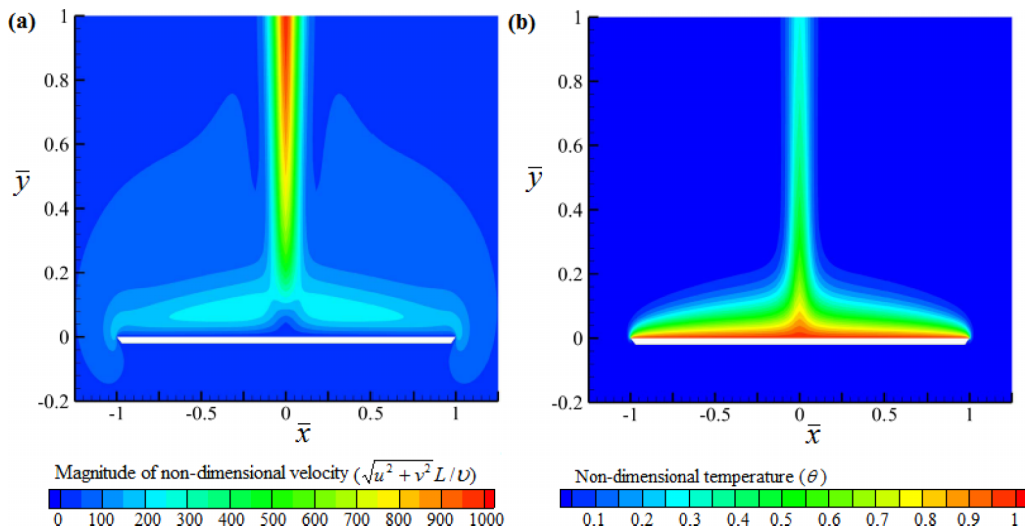


FIG. 4. Contours of velocity magnitude and temperature obtained by 2-D CFD simulations for a finite plate: (a) non-dimensional velocity magnitude and (b) non-dimensional temperature (all results correspond to $Gr = 2 \times 10^6$ and $Pr = 0.7068$).

y -direction is relatively small as compared to the boundary-layer regions (Figure 4(b)). Many details about a laminar plume developed over a horizontal line source are discussed in Refs. 29 and 30 (dynamics of plumes in turbulent thermal convection can be found in Refs. 31–33).

Figure 4(a) also shows two wing-shaped boundary layers which are developed above the heated surface. u (parallel to the hot surface) is the major component of velocity within the boundary layers. Near the leading edges of the plate (i.e., $\bar{x} = 1$ and $\bar{x} = -1$), the velocity boundary layers are distorted due to the edge effect. In the case of thermal boundary layers (see Figure 4(b)), such distortion near the edges is comparatively small. From the leading edge towards the plume, the thickness of boundary layers increases. In the y -direction, with increasing distance from the heated surface, the temperature decreases, whereas, velocity first increases to attain a maximum value and then onward decreases. Some other flow features related to velocity and thermal boundary layers are described in Section IV B.

Another region shown in Figure 4 is the junction between boundary layer regions and the plume. To describe an axi-symmetric plume above a planar boundary, Whittaker and Lister³⁴ called the junction the “turn-round region”. According to them, the flow within boundary layers feeds the plume through the turn-round region; and, in the turn-round region, the effect of advection predominates over the effect of diffusion. Fluid streams, from two opposite ends of the plate, move towards the plane of symmetry. However, prior to vis-à-vis collision, flow separation takes place. It is already mentioned that within the boundary layers, the major component of velocity is u , whereas within the plume, the major component of velocity is v .

B. Two-dimensional CFD solutions versus similarity solutions

Similarity solution above a horizontal heated plate is available in Refs. 6 and 14–16. According to Rotem and Claassen,¹⁶ it is possible to achieve self-similar solution in the case of a “semi-infinite” plate (a plate with only a single leading edge) because of the absence of a characteristic length. The present CFD study focuses on finite plates. For finite horizontal plates, near the central region, the boundary layer approximations collapse due to the existence of a plume, as described in Section IV A. Therefore, it is expected that the similarity theory does not hold there. However, the prediction of similarity theory may be accurate within the boundary layers. It will be interesting to examine the applicability area of similarity solution above a finite horizontal heated line. To fulfil this objective, some special tests are carried out in this section.

The similarity equations are as follows:

$$5F''' + 3FF'' - F'^2 = 2(G - \eta G'), \quad (14)$$

$$H = G', \quad (15)$$

$$H'' + 3/5Pr FH' = 0. \quad (16)$$

The boundary conditions required to solve Equations (14)-(16) are given below,

$$\text{at } \eta = 0, F = F' = 0, H = G' = 1, \quad (17)$$

$$\text{as } \eta \rightarrow \infty, F' = 0, G = 0, H = 0. \quad (18)$$

Full derivation of Equations (14)-(16) and the method for solving these equations are given in Refs. 6 and 16. Such details are therefore not included here. Only the information, which is necessary for the present discussion, is given below.

While deriving the similarity equations all previous researchers consider that the plate is “semi-infinite,” and the origin is set at the leading edge of the plate. The corresponding abscissa is denoted by x' (shown in Figure 1). The non-dimensional x' -coordinate is denoted by \bar{x}' ($\bar{x}' \equiv x'/L^*$, for a 1-D finite plate $L^* = L$). In Equations (14)-(18), the variables F , G , and H are, respectively, non-dimensional stream function, non-dimensional pressure, and non-dimensional temperature. F , G , and H are functions of η only. The expression of the similarity variable η is as follows:

$$\eta = \bar{y} Gr^{1/5} (\bar{x}')^{-2/5}. \quad (19)$$

The other useful relations, which are adopted from the similarity theory, are given below,

$$\begin{aligned} F'(\eta) &= \bar{u}Gr^{-2/5}(\bar{x}')^{-1/5}, \\ H(\eta) &= \theta. \end{aligned} \quad (20)$$

For particular values of Gr and Pr , F' and H can also be calculated by present CFD simulations. However, it cannot be claimed that F' and H obtained by the CFD simulations are the functions of η only. Therefore, instead of using $F'(\eta)$ and $H(\eta)$, the notations F' and H are used while comparing CFD solutions with similarity solutions.

In the y -direction, with increasing distance from the heated surface (at $\bar{y} = 0$), \bar{u} increases to attain a maximum value and then onward decreases (Figure 3(c)). At any \bar{x}' , there is a particular \bar{y} where \bar{u} attains \bar{u}_m (the maximum value of \bar{u}). The locus of these \bar{y} and the corresponding values of \bar{u}_m are calculated by CFD simulations. Then these \bar{y} coordinates are converted into η (by Equation (19)) and the corresponding \bar{u}_m are converted into F' (by Equation (20)). η_m represents the values of η corresponding to the maxima, and $F'_{\eta,m}$ is the values of F' at η_m . Figure 5(a) shows $F'_{\eta,m}$ versus \bar{x}' and η_m versus \bar{x}' obtained from computation performed at $Gr = 2 \times 10^6$ and $Pr = 0.7068$ (input parameters are given in Table I). The same figure also includes the predictions of the similarity theory. In the similarity solution, $F'_{\eta,m}$ and η_m are independent of \bar{x}' . On the other hand, the CFD solutions (for $F'_{\eta,m}$ and η_m) depend on \bar{x}' . Near the leading edge ($\bar{x}' = 0$) and near the plane of symmetry ($\bar{x}' = 1$), both $F'_{\eta,m}$ and η_m vary steeply. Such trends appear because of the edge effect near $\bar{x}' = 0$ and the development of plume near $\bar{x}' = 1$. A flattish trend can be seen between the plume and the zone affected by the edge effect. However, in the region of the flattish trend, the computed values of η_m and $F'_{\eta,m}$ are greater than their respective self-similar values. For a particular Pr , if Gr increases the values of η_m and $F'_{\eta,m}$ within the flat portion approach to their respective self-similar values (see Figures 6(a) and 6(b)).

It is inappropriate to interpret F' as a non-dimensional x -velocity without understanding the role of $(\bar{x}')^{-1/5}$ in Equation (20). For a large Gr , let us explore the role of $(\bar{x}')^{-1/5}$. When $\bar{x}' \rightarrow 1$, the term $(\bar{x}')^{-1/5}$ also tends to 1. $F'_{\eta,m}$ is very small because of the presence of $Gr^{-2/5}$ in Equation (20). When $\bar{x}' \rightarrow 0$, $F'_{\eta,m}$ is finite but large (see Figure 6(b)), and the value of $F'_{\eta,m}$ depends on both $(\bar{x}')^{-1/5}$ and $Gr^{-2/5}$. It is expected that near leading edge ($\bar{x}' \rightarrow 0$), x -velocity is small; but one may conclude the reverse by interpreting F' as a non-dimensional x -velocity.

It is interesting to calculate the local temperature at the locus of maximum x -velocity. Figure 5(b) shows the non-dimensional temperature H (from $\bar{x}' = 0$ to $\bar{x}' = 1$) at the locus of \bar{u}_m . The same figure also includes the prediction of the similarity theory (which is independent of \bar{x}'). It is observed that in direction of \bar{x}' , the computed values of H vary steeply near $\bar{x}' = 0$ and near $\bar{x}' = 1$. However, between $\bar{x}' \approx 0.3$ and $\bar{x}' \approx 0.8$, a flattish trend is obtained. The computed values of H in the flattish zone are less than the self-similar value. For a fixed Pr , if Gr increases the values of H within the flat portion approach to their respective self-similar values (Figure 6(c)).

Figures 7(a) and 7(b), respectively, display the η -variation of F' and the η -variation of H at three \bar{x}' -locations ($\bar{x}' = 0.1$, $\bar{x}' = 0.5$, and $\bar{x}' = 0.9$). [The η variations are shown here to explore the y -profiles of the non-dimensional quantities.] The same figures also include the prediction of the similarity theory. Figure 7(a) shows that at large η , the values of F' are nonzero at all three locations. The non-zero values occur due to the horizontal diffusion described in Section IV A. The similarity theory is incapable of capturing this effect (Equation (18)). Therefore, for a large η , the prediction of similarity is diverted from the prediction of CFD even at $\bar{x}' = 0.5$ where boundary layer exists (Figures 4 and 7(a)).

The following observations can be extracted from Figure 7(b). At $\bar{x}' = 0.9$, H is much greater than zero (or, T_∞ is not attained) even at $\eta = 12$. This occurs because of the presence of plume. At $\bar{x}' = 0.5$ (a region within boundary layer), the profile of H obtained by CFD is in good agreement with the similarity profile. The computed H -profile does not vary significantly while \bar{x}' increases from 0.1 (near the leading edge) to 0.5.

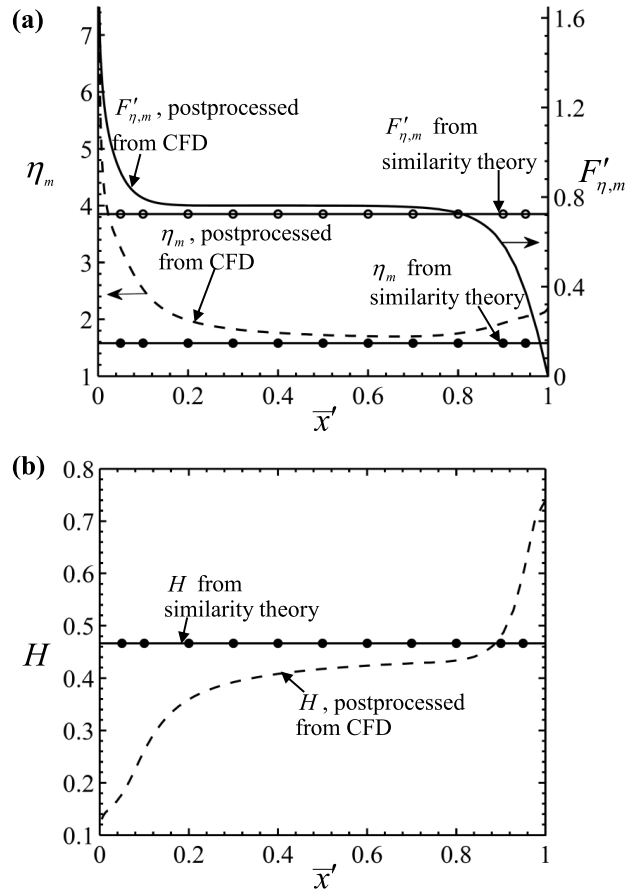


FIG. 5. Predictions of 2-D CFD solutions for a finite plate versus predictions of the similarity theory: \bar{x}' -variation of non-dimensional parameters at the locus of \bar{u}_m . (a) Variation of $F'_{\eta,m}$ and η_m and (b) variation of H (all results correspond to $Gr = 2 \times 10^6$ and $Pr = 0.7068$).

V. RESULTS OF 3-D CFD SIMULATIONS

In this section, the results of the present 3-D CFD simulations are presented and critically analysed. In order to streamline the physical understanding, the analysis is grouped in Subsections V A–V E. Effects of finiteness on the thermo-fluid-dynamics of natural convection above heated planforms are assessed in these subsections.

A. Velocity and temperature distributions above an isothermal square plate

In this section, the results for a representative 3-D CFD simulation, which is performed for a square plate, are described. Each side of the square plate (α) is 0.2 m. Isothermal conditions are specified at the top surface of the plate and T_w equals 315.5 K. Other surfaces are insulated. p_∞ and T_∞ are 101 325 Pa and 300 K, respectively. Air is used as working fluid ($Pr = 0.7068$). The reference length L^* is considered as $\alpha/2$ to maintain consistency with the reference scale used for 1-D plate (Section IV). Gr , for the given geometry and operating conditions, is 2×10^6 (calculated by Equation (12)). Among the output variables, the discussion in this section will be focused on the in-plane velocity, out-of-plane velocity, and temperature. The variations of these three variables in the three-dimensional space are described below.

The isothermal surface (at $\bar{y} = 0$) is parallel to a (x, z) plane (gravity is acting in the negative y -direction). The extent of the isothermal surface is $-1 \leq x \leq 1$ and $-1 \leq z \leq 1$. In-plane velocity is the resultant of u and w . Here, the magnitude of in-plane velocity is denoted by V_{ip} . V_{ip}

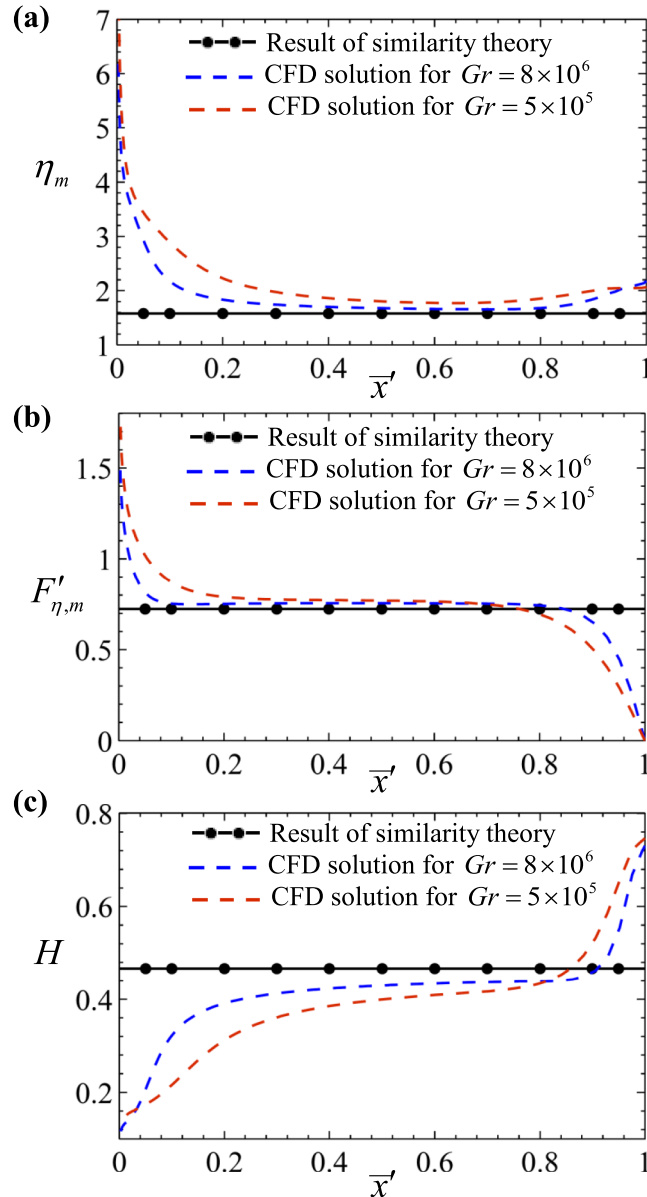


FIG. 6. Effect of change in Grashof number (Gr) reflected at the locus of \bar{u}_m : prediction of 2-D CFD simulations for a finite plate. (a) Variation of η_m ; (b) variation of $F'_{\eta,m}$; (c) variation of H (all results correspond to $Pr = 0.7068$).

equals $\sqrt{(u^2 + w^2)}$. V_{ip} is non-dimensionalized according to the relation $\bar{V}_{ip} \equiv V_{ip}\alpha/(2\nu)$. In the three-dimensional plots given below, the orientations of the three coordinates are selected such that the flow features can be visualized most clearly.

Figure 8 shows the iso-surfaces of \bar{V}_{ip} obtained from the CFD simulations. The development of boundary layers, the interactions of the boundary layers and the zones of high and low \bar{V}_{ip} can be observed in this figure. Due to no-slip condition, the value of \bar{V}_{ip} very close to the isothermal surface is very small. This is reflected in Figure 8(f). Figures 8(a) and 8(b) show the zones of high \bar{V}_{ip} . It can be seen that these zones are four discrete triangular surfaces. Figure 8(a) shows that very high \bar{V}_{ip} exists at a considerable distance from the plate edges. At the middle portion of the square surface, \bar{V}_{ip} is small due to the development of plume; therefore, the surfaces of high \bar{V}_{ip} do not occupy the middle portion of the plate (see Figures 8(a) and 8(b)). It can be observed that \bar{V}_{ip} is

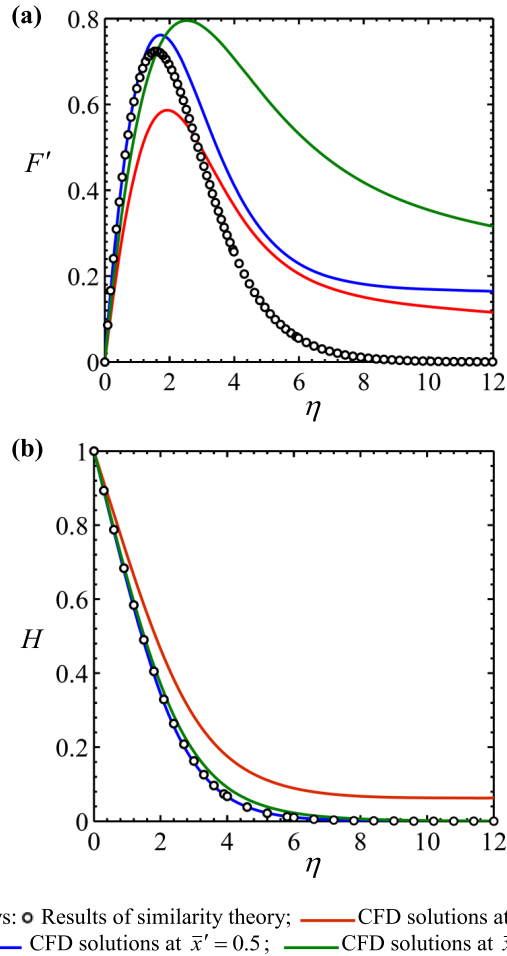


FIG. 7. Predictions of 2-D CFD solutions for a finite plate versus predictions of the similarity theory: η -variation of non-dimensional parameters at three representative values of \bar{x}' . (a) η -variation of F' ; (b) η -variation of H (all results correspond to $Gr = 2 \times 10^6$ and $Pr = 0.7068$).

not large at the diagonals (Figures 8(a) and 8(b)). This is so because u and w are mutually perpendicular, and the interaction of the mutually perpendicular streams is such that in-plane velocity is converted into out-of-plane velocity. It can be seen, from Figures 8(a)–8(e), that with a progressive decrease of the iso-values, the iso-surfaces are shifted towards a higher y -coordinate, the surfaces are distorted and the surfaces enlarge to engulf the four edges of the plate. The shift towards a higher y -coordinate can be explained from the fact that after attaining a maxima, u and w decrease in the y -direction. Near the edges the in-plane velocity is small; therefore, the edges of the plate are covered with the low valued iso-surfaces. Figures 8(d) and 8(e) show that at a large \bar{y} , nonzero \bar{V}_{iD} exists to feed the plume by horizontal diffusion.

Figure 9 shows the iso-surfaces of non-dimensional out-of-plane velocity (\bar{v}). The reasons for the development of \bar{v} for a finite plate are discussed in Section IV. The plume on a 1-D plate described in Section IV is originated because of the presence of two opposing streams. On the other hand, for a square plate, four separate streams, which evolve near the four edges of the isothermal surface and spatially transform into four boundary layers, are involved in the development of a plume. The interaction of the mutually perpendicular streams along the diagonal of the square plate, which leads to a conversion of in-plane velocity to out-of-plane velocity, is reflected in the shape of the plume (see Figures 9(d) and 9(e)). It is seen that around the centre of the plate, the value of \bar{v} is high (Figures 9(a) and 9(b)). However, the bottom-most position of the plume is seen to occur at a distance above the heated surface as a consequence of the existence of the turn-round

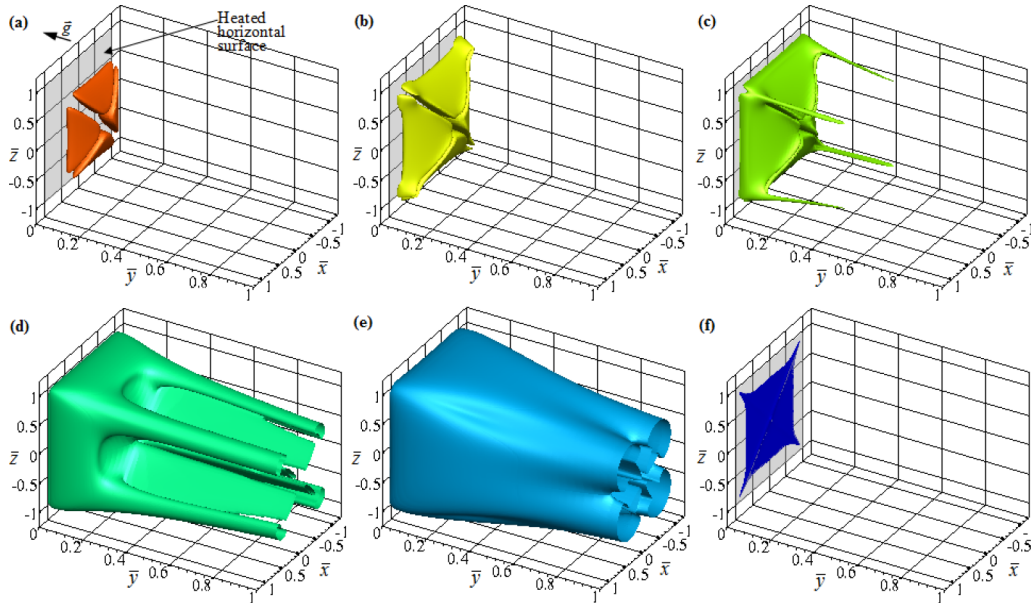


FIG. 8. Distribution of non-dimensional in-plane velocity (\bar{V}_{ip}) in the three-dimensional space above an isothermal horizontal surface obtained by 3-D CFD simulations. (In the above representation, the horizontal surface is rotated 90° for the ease of visualization. Gravity is acting in the negative y -direction.) Values of iso-surfaces: (a) 202; (b) 170; (c) 160; (d) 85; (e) 55; and (f) 9.

region described in Section IV A. The core of plume, where \bar{v} is large, is captured in Figure 9(a). Figures 9(b) and 9(c) show that with an increase in distance (in the $x-z$ plane) from the centre of the square, \bar{v} decreases; and, the iso-surfaces are extended diagonally. The iso-surfaces representing moderate to low \bar{v} are displayed in Figures 9(d)–9(f). It can be seen that with decreasing \bar{v} , the bottom of the iso-surfaces moves closer to the square plate.

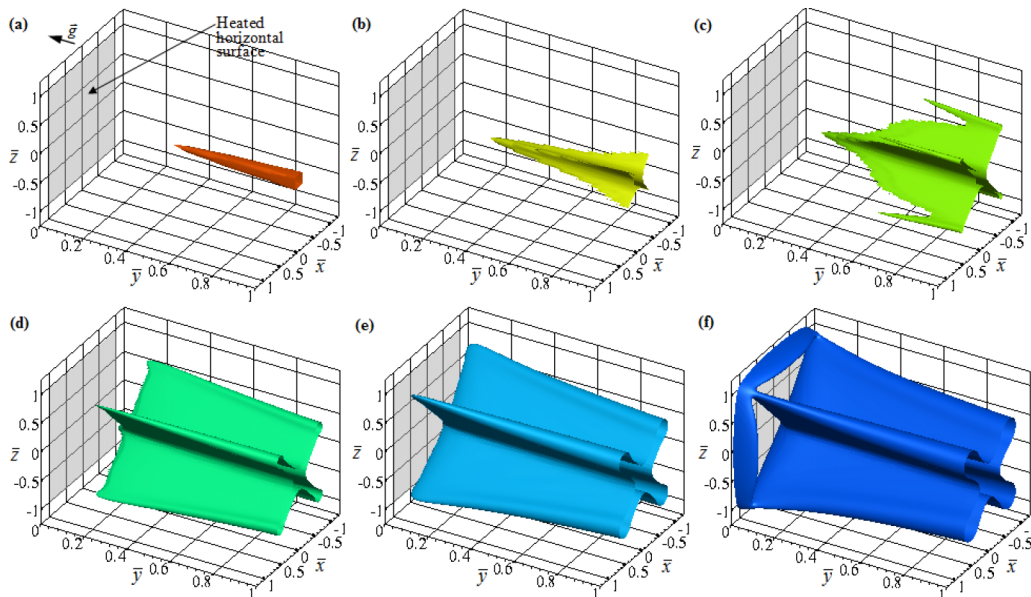


FIG. 9. Distribution of non-dimensional out-of-plane velocity (\bar{v}) in the three-dimensional space above an isothermal horizontal surface obtained by 3-D CFD simulations. (In the above representation, the horizontal surface is rotated 90° for the ease of visualization. Gravity is acting in the negative y -direction.) Values of iso-surfaces: (a) 910; (b) 750; (c) 650; (d) 400; (e) 140; and (f) 40.

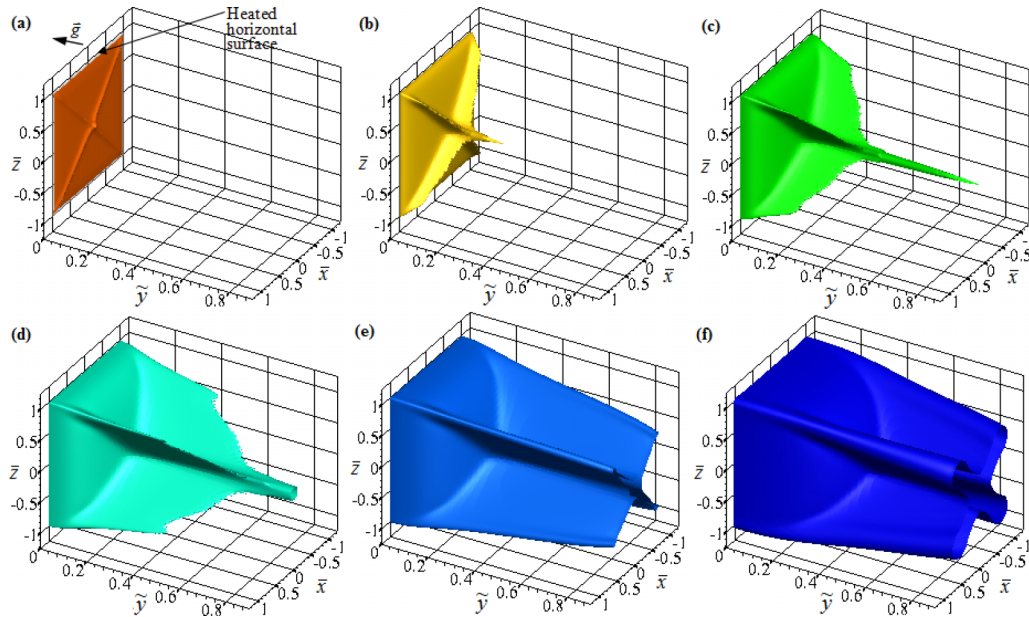


FIG. 10. Distribution of non-dimensional temperature (θ) in the three-dimensional space above an isothermal horizontal surface obtained by 3-D CFD simulations. (In the above representation, the horizontal surface is rotated 90° for the ease of visualization. Gravity is acting in the negative y -direction. \tilde{y} is a modified coordinate to amplify the details near the isothermal surface.) Values of iso-surfaces: (a) 0.97; (b) 0.8; (c) 0.55; (d) 0.32; (e) 0.14; and (f) 0.01.

A comparison of Figures 8 and 9 reveals that, in general, the in-plane velocity is low in regions where the out-of-plane velocity is high. Another important feature of the flow field is that the magnitude of maximum out-of-plane velocity is much greater than the maximum in-plane velocity.

Figure 10 shows the spatial distributions of the non-dimensional temperature (θ). The value of θ is 1 at the isothermal surface and, θ decreases in the y -direction. In order to examine the subtle details of the variation of temperature close to the surface, the y -coordinate is non-linearly stretched using the transformation $\tilde{y} \equiv 1 - 10^{-\tilde{y}}$ and this modified y -coordinate \tilde{y} is shown in Figure 10. Figure 10(a) displays the zone of high temperature. The protuberant diagonal lines in Figure 10(a) appear due to small in-plane velocity (and moderate out-of-plane velocity) along the diagonals. The peaked protrusions of iso-temperature-surface along diagonals in Figures 10(b)–10(d) signify that the temperature distribution is non-uniform at any (x, z) plane above the square plate (though uniform temperature distribution is specified at $\tilde{y} = 0$). The temperature within the four velocity boundary layers is smaller than the temperature near diagonals and that near the centre of the square. This enhances the non-uniformity in temperature distribution at any (x, z) plane.

The in-plane velocity is very small and out-of-plane velocity is very large at the central portion of the square. Consequently, in the central portion of the plate, the hot fluid close to the isothermal surface is convected upwards. The needle shaped protrusions in the iso-temperature-surface shown in Figures 10(b) and 10(c) are attributed to this fact. With a progressive decrease in θ , the following sequential observations can be made. At first, the head of the needle enlarges and takes a round shape (Figure 10(d)), and then the round shaped head extends along diagonals and takes a star shape (Figures 10(e) and 10(f)). Moreover, the base of the iso-temperature-surface bulges towards the centre of the plate in a similar manner as the velocity boundary layer grows.

B. Rectangular planform and the effects of geometry

In this section, CFD simulations are performed for rectangular plates of various aspect ratios. The top surface of the plate is isothermally heated and all other surfaces are insulated. Consider that the lengths of any two adjacent sides of the isothermal surface are a and b and $a > b$. The aspect

TABLE IV. Effect of varying aspect ratio by two different methods.

Aspect ratio ($\phi \equiv a/b$)	Dimensions of plates used in method 1			Nu obtained by method 1	Dimensions of plates used in method 2			Nu obtained by method 2
	a (m)	b (m)	Θ		a (m)	b (m)	Θ	
1	0.2	0.2	0.050	13.67	0.2	0.2	0.050	13.67
2	0.4	0.2	0.067	12.26	$0.2 \times \sqrt{2}$	$0.2/\sqrt{2}$	0.047	14.15
4	0.8	0.2	0.080	11.56	0.4	0.1	0.040	15.26
8	1.6	0.2	0.089	11.20	$0.2 \times 2\sqrt{2}$	$0.2/(2\sqrt{2})$	0.031	17.00
16	3.2	0.2	0.094	11.03	0.8	0.05	0.024	19.06

ratio is denoted by ϕ ($\phi \equiv a/b$). Here, two different methods are employed to vary the aspect ratio of the plate. In method 1, b is kept fixed and a is varied with consequent change in surface area. In method 2, the area of the isothermal surface is kept fixed, and the aspect ratio (ϕ) is varied by varying b and a simultaneously. For consistent book-keeping, the case $\phi = 1$ represents the same reference square plate for both methods. The absolute dimensions of the reference square plate and the operating conditions (T_w , T_∞ , p_∞ , and Pr) are as specified in Section V A.

Table IV contains the dimensions of the plates for various aspect ratios (ϕ) according to methods 1 and 2. Three-dimensional computational simulations are run for each of these rectangular surfaces. The computed values of Nu are given in Table IV. The same value of reference length (equal to half of the length of a side of the reference square plate, i.e., 0.1 m) is used for the calculation of all Nusselt numbers given in Table IV, so that the Nusselt number becomes directly indicative of the surface heat flux and a comparison of computed area-averaged heat flux is possible.

It can be seen from Table IV that the two methods produce mutually opposite trends in the variation in area-averaged surface heat flux as the aspect ratio ϕ is altered. Method 1 predicts that Nu (and therefore, the area-averaged surface heat flux) decreases with an increase in ϕ . On the contrary, method 2 predicts that Nu (and therefore, the area-averaged surface heat flux) increases with an increase in ϕ . To resolve this apparent dichotomy a new parameter Θ needs to be invoked. Θ is defined as

$$\Theta = A/\Pi, \quad (21)$$

where A is the area of the isothermal surface and Π is the surface perimeter encompassing the surface area.

It can be observed from Table IV that, for both methods 1 and 2, Nu (and therefore, the area-averaged surface heat flux) increases with a decrease in Θ . The physical significance of this trend is that for a fixed cross-sectional area of an isothermally heated horizontal surface, the surface heat flux increases with an increase in the perimeter. Two limiting values of Θ are, respectively, $b/4$ (for $\phi = 1$, i.e., a square surface) and $b/2$ (for $\phi \rightarrow \infty$). The representative results shown in Table IV encapsulate a wide range of Θ . For example, the results presented for method 2 cover a range from $\Theta = b/4$ to $\Theta = b/2.08$.

C. Distributions of surface heat flux on heated rectangular and square planforms

In this section, it is shown that the distributions of surface heat flux on a heated isothermal surface depend on the aspect ratio (ϕ). For this purpose, two representative plate-geometries are selected. One of these two is a square plate ($\phi = 1$) whose geometry is the same as given in Section V A (each side equals 0.2 m). The other is a rectangular plate ($\phi = 4$) for which $a = 0.8$ m and $b = 0.2$ m. Three-dimensional CFD simulations for both square and rectangular plates are carried out under the same operating condition (T_w , T_∞ , p_∞ and Pr) as specified in Section V A.

Figure 11 shows the distribution of non-dimensional surface heat flux on the square and rectangular planforms. The difference between Figures 11(a) and 11(b) is striking, but the figures

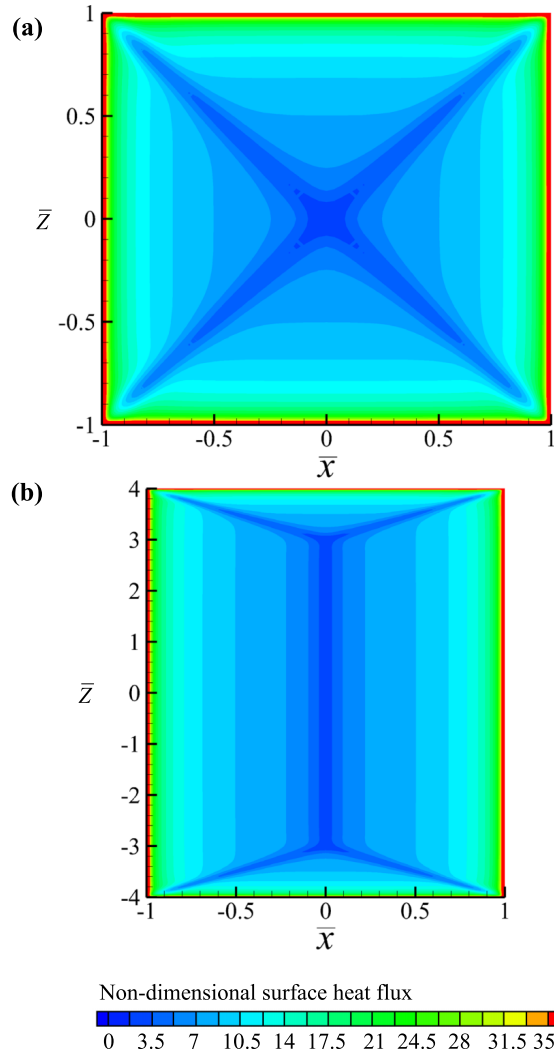


FIG. 11. Distributions of non-dimensional surface heat flux on a square planform and a rectangular planform: predictions of 3-D CFD simulations. (The scales used for the abscissa and ordinate are varied to reveal the details of the heat flux contours.) (a) Square planform ($\phi = 1$) and (b) rectangular planform ($\phi = 4$).

also offer a visual clue as to how one solution transforms into the other when the aspect ratio is altered.

The expression of non-dimensional surface heat flux (\bar{q}_w) is as follows:

$$\bar{q}_w = q_w(b/2)/(k(T_w - T_\infty)), \quad (22)$$

where q_w is the dimensional surface heat flux. It is to be noted that q_w is the local surface heat flux (q_w is not the area-averaged value of surface heat flux). Figure 11(a) (square) and Figure 11(b) (rectangular) show that near the edges of both square and rectangular plates, \bar{q}_w is large. For the sake of representing the gradation of contours distinctly, the values of \bar{q}_w , shown in Figures 11(a) and 11(b), are kept below 35. (The actual values of maxima obtained from CFD solutions are greater than 35, and the maxima for the rectangular surface is greater than the maxima for the square surface.)

The shape of low- \bar{q}_w -zone on the heated square surface is very different from the shape of low- \bar{q}_w -zone on the heated rectangular surface. The strength of convection is small in the low- \bar{q}_w -zones. For both square and rectangular surfaces, the low- \bar{q}_w -zones have a central part and four limbs. The four limbs develop due to the presence of four physical corners. The central part

indicates the location of the turn-round region which is fed by mutually perpendicular streams within four separate boundary layers. The conversion of in-plane velocity to out-of-plane velocity causes low convection in the central part and four limbs. The low- \bar{q}_w -zone on the heated square surface is star-shaped. The central part of the star-shaped low- \bar{q}_w -zone is also star-shaped and occupies a small region. Most of the region of the low- \bar{q}_w -zone is occupied by the four limbs. On the contrary, for the heated rectangular surface, the central part of low- \bar{q}_w -zone is large and the limbs are small. The central part is rectangular-shaped. The small limbs and large central part signify that the convective flow originated from the shorter sides of the rectangular surface has small contribution in the overall surface heat flux. The overall surface heat flux is, therefore, predominately governed by the convective heat flux originated near the edges of longer sides of the rectangular surface. The above understanding of the flow physics helped us to deduce a new theoretical correlation for predicting the averaged surface heat flux for various rectangular surfaces (whose aspect ratio varies from 1 to ∞) over a wide range of Grashof number (see Section V D).

D. A generic theoretical correlation for predicting Nusselt number

A theoretical correlation, by which the Nusselt number for various aspect ratios (from $\phi = 1$ to $\phi \rightarrow \infty$) over a large range Grashof number can be predicted, is given in this section. (It is to be noted that throughout the paper the Nusselt number, which is used, is as an area-averaged quantity.) It is shown here that the Nusselt number obtained from the more computationally demanding 3-D simulations can be predicted with sufficient accuracy by the theoretical correlation.

In Section V C, the contours of \bar{q}_w on a heated rectangular surface ($\phi = 4$) are shown. It is mentioned that the overall surface heat flux is predominately governed by the convective flux originated near the edges of longer sides (Section V C) of the rectangular surface. This dominance enhances with an increase in ϕ (while keeping the length of the shorter sides fixed). When ϕ is large the contribution of shorter sides is confined in the neighborhood of the corners of the rectangular surface. Therefore, in the limit of $\phi \rightarrow \infty$, although 2-D simulations cannot capture the effect of physical corners, the overall heat transfer obtained by 3-D simulations can be effectively estimated with computationally less expensive 2-D simulations.

A comparison of similarity solutions with the predictions of 2-D simulations is provided in Section IV B. It is shown that there exists a region above a heated horizontal line where the temperature distribution predicted by similarity theory is approximately valid over a range of Grashof number (see Figure 6(c)). At this region, the surface heat flux obtained by 2-D simulations is comparable to that obtained by similarity theory. Figure 11(b) shows that near the edges, non-dimensional surface heat flux (\bar{q}_w) is large. There, the value of \bar{q}_w is much greater than the self-similar value. On the other hand, at the middle portion of the rectangular surface (low- \bar{q}_w -zone), \bar{q}_w is smaller than the self-similar value. The integrated effect (considering the full extent of the heated surface) is such that over a large range of Grashof number, the area-averaged \bar{q}_w obtained by 2-D simulations is close to the area-averaged \bar{q}_w obtained by similarity theory (this fact will be demonstrated below). Therefore, when the aspect ratio is large, the Nusselt number predicted by the similarity theory is close to the Nusselt number obtained by 3-D simulations; this fact is true over a large range of Grashof number. This observation indicates the possibility of modifying the similarity theory for predicting the Nusselt number over a large range Grashof number at other aspect ratios.

The expression of the Nusselt number, according to the similarity theory,⁶ is as follows:

$$Nu_s = C_s Gr_s^{1/5}. \quad (23)$$

The subscript s is used here to denote similarity theory. The coefficient C_s is a function of Pr and is given by

$$C_s = -5/3H'(0). \quad (24)$$

Equation (23), derived by the similarity theory, is approximately applicable for a large aspect ratio rectangular planform ($\phi \rightarrow \infty$) due to the reasons mentioned above. Equation (23) can be expanded

into the following form:

$$h_{avg}(b/2)/k = C_s \left[\frac{g\beta(L_{eff})^3(T_w - T_\infty)}{\nu^2} \right]^{1/5}, \quad (25)$$

where $L_{eff} = b/2$. The purpose of using the new parameter L_{eff} in Equation (25) is to explore ways to make the equation generically applicable for any rectangular planform with arbitrary aspect ratio ($1 \leq \phi < \infty$).

Refer to the method 1 described in Section V B in which various values of ϕ are obtained by altering the longer side of the rectangle a and keeping b fixed. The LHS of Equation (25) represents the Nusselt number, and for the time being, a reference length $b/2$, which is the half width of the rectangular planform, is used to define the Nusselt number. L_{eff} , in the RHS of Equation (25), signifies an effective path-length along which buoyancy driven fluid particles, starting from the edges of the planform, travel against the viscous force to arrive at the central-region of the planform. For a large aspect ratio rectangular planform, most of the fluid particles enter through the long edges (of length a) and travel an effective path length of $b/2$ before being engulfed into the central plume; L_{eff} is, therefore, approximately equal to $b/2$. On the other hand, for a square planform ($a = b$ and $\phi = 1$), all four edges contribute equally. Thus, for a square planform,

$$[L_{eff}]_{square} = \sqrt{(b/2)^2 + (b/2)^2}, \quad (26)$$

i.e., $[L_{eff}]_{square}$ is the half of the length of the diagonal of the square.

For any arbitrary rectangular planform ($1 < \phi < \infty$), such an effective length scale cannot be directly determined because the contributions of the two unequal sides are different ($a > b$). It is easy to argue that the effective length for an arbitrary rectangle is not equal to half the length of the diagonal ($[L_{eff}]_{rect} \neq 0.5L_{diagonal}$). This can be appreciated by determining the limiting value: $L_{t\phi \rightarrow \infty} L_{diagonal} = L_{t\phi \rightarrow \infty} a\sqrt{(1 + 1/\phi^2)} = a$. But we have shown from physical argument that, in this limiting case, $L_{t\phi \rightarrow \infty} [L_{eff}]_{rect} = b/2$. This problem is resolved here by constructing a reference square whose each side is equal to the longer side of the original rectangle (i.e., a). We now make a hypothesis that the effective length for the original rectangle is $1/\phi$ times the length of the diagonal of the reference square (the hypothesis being based on properties of similar triangles),

$$[L_{eff}]_{rect} = [L_{eff}]_{ref, square}/\phi. \quad (27)$$

Furthermore, it is to be realized that the distribution of surface heat flux on a heated rectangular planform depends on the relative proportion of fluid flux supplied by any two unequal sides of the planform. However, for the reference square, all sides being equal, such relative proportions of fluid flux and corresponding distribution of surface heat flux will be different from those obtained for the case of original rectangular planform. On account of this fact, a weighting factor w_f ($w_f = 1/\phi$) is invoked in the definition of $[L_{eff}]_{ref, square}$ to mimic the original distribution of heat flux. Thus,

$$[L_{eff}]_{ref, square} = \sqrt{(a/2)^2 + w_f(a/2)^2}. \quad (28)$$

With $w_f = 1/\phi$ and the relation $a = \phi b$, Equation (28) becomes

$$[L_{eff}]_{ref, square} = \sqrt{\phi^2(b/2)^2 + \phi(b/2)^2}. \quad (29)$$

Now substituting Equation (29) in Equation (27), we have

$$[L_{eff}]_{rect} = (b/2)\sqrt{(\phi + 1)/\phi}. \quad (30)$$

Equation (30) has the property that it behaves properly in both limits. When $\phi = 1$, Equation (30) shows that $[L_{eff}]_{rect} = b/\sqrt{2} = a/\sqrt{2}$, recovering the result for a square. As $\phi \rightarrow \infty$, Equation (30) gives $L_{t\phi \rightarrow \infty} [L_{eff}]_{rect} = b/2$ which is physically realistic.

So far in this paper, the half-width of the plate (i.e., $b/2$) is used as a reference length scale for defining the Nusselt number. This provided a consistent platform to conduct comparative studies involving similarity theory, 2-D and 3-D CFD simulations, and shape variation according

to method 1 and method 2. However, according to Goldstein *et al.*,³⁵ Θ (the ratio of surface area and perimeter) should be adopted as the physical length scale for generalized representation of natural convection results. We, therefore, recast our theoretical correlation for the Nusselt number, Equation (25), such that the same length scale Θ is used in both sides of the equation.

The mathematical relation between $b/2$ and Θ is as follows:

$$b/2 = \left(\frac{\phi + 1}{\phi} \right) \Theta. \quad (31)$$

The generic length scale Θ varies with a change in aspect ratio ϕ . For $\phi = 1$ (square plate), the value of Θ is $b/4$, and for $\phi \rightarrow \infty$, the value of Θ is $b/2$ (see Equation (31)). It is to be noted that for $\phi \rightarrow \infty$, the generic scale Θ totally corresponds to the scale that was used to represent the results of 2-D simulations and similarity.

Now, using Equations (30) and (31), the effective length scale for Grashof number can be expressed in the following form:

$$L_{eff} = \left(\frac{\phi + 1}{\phi} \right)^{3/2} \Theta. \quad (32)$$

The subscript ‘‘rect’’ in $[L_{eff}]_{rect}$ is dropped while writing Equation (32) because Equation (32) is also valid for a square planform. Substitution of the expression of L_{eff} (Equation (32)) and the expression of $b/2$ (Equation (31)) in Equation (25) leads to

$$Nu^* = C_s \left(\frac{\phi}{\phi + 1} \right)^{1/10} (Gr^*)^{1/5}, \quad (33)$$

where

$$Nu^* = h_{avg} \Theta / k \quad (34)$$

and

$$Gr^* = \frac{g \beta \Theta^3 (T_w - T_\infty)}{\nu^2}. \quad (35)$$

In Equation (33), C_s is specified by the similarity theory and is independent of ϕ . For $Pr = 0.7068$ (air as the working fluid), the value of $H'(0)$ is 0.356; and, C_s equals 0.593.

Equation (33) is the generic theoretical correlation for the Nusselt number established in the present work. Even though a scaling hypothesis is used in its derivation, no empiricism or regression analysis is used. The exponents (such as the 1/5th power of the Grashof number) or the coefficient (C_s) in the formula are all determined theoretically. The new physical understanding that could be crystallized from the present CFD simulations was useful in formulating the scaling hypothesis, but any numerical values obtained from CFD simulations or any empirical values obtained from experiments have not been used in the derivation of Equation (33). Rather, the validity of Equation (33) is assessed by comparing its predictions with the results of present 2-D and 3-D CFD simulations.

The applicability of Equation (33) at various values ϕ is examined over a wide range of Gr_s ($Gr_s \equiv g \beta (b/2)^3 (T_w - T_\infty) / \nu^2$). Table V shows three representative Gr_s for which three clusters of calculations are performed. For each cluster, b is kept at a fixed value. All other relevant input parameters are given in Table V. The results of the three set of calculations are displayed in Figure 12. For each Gr_s , the results displayed in Figure 12 contain the predictions of Equation (33), similarity theory, 2-D simulations, 3-D simulations and the experimental correlation of Fishenden and Saunders.¹⁸

Fishenden and Saunders¹⁸ obtained the correlation for a heated square plate ($\phi = 1$). The correlation is as follows:

$$Nu^* = 0.38 (Gr^* Pr)^{1/4}. \quad (36)$$

Prediction of Equation (33) at $\phi = 1$ is tested with the experimental correlation given by Fishenden and Saunders¹⁸ (Equation (36)). At $Gr_s = 10^5$, the prediction of Equation (33) agrees well with the

TABLE V. Input parameters for three representative set of calculations used to demonstrate the utility of the generic theoretical correlation (Equation (33)).

Cluster	Gr_s	Aspect ratio ($\phi \equiv a/b$)	Θ	b (m)	Working fluid	Other operating conditions
1	2×10^6		0.05–0.0941	0.2		$p_\infty = 101\,325$ Pa;
2	1×10^5	1–16	0.0184–0.0346	0.0736	Air	$T_w = 315.5$ K;
3	1×10^4		0.0085–0.0161	0.0342		$T_\infty = 300$ K

prediction of Equation (36). A small mismatch between the prediction of Equation (33) and the prediction of Equation (36) is found at $Gr_s = 10^4$ and $Gr_s = 2 \times 10^6$. It can be seen from Figure 12 that over a wide range of Gr_s and ϕ , the prediction of the present theoretical correlation (Equation (33)) agrees well with the results obtained by the present 3-D CFD simulations, thus giving confidence in the theoretical correlation. Predictions of Equation (33) at a large ϕ (up to $\phi = 16$ shown in Figure 12) is compared with the predictions of 2-D CFD simulations and similarity theory. It can be seen that at each Gr_s , Nu^* obtained by 2-D CFD simulations are very close to Nu^* obtained by similarity theory. Figure 12 displays that when ϕ is large the prediction of Equation (33) (and the prediction of 3-D simulations) asymptotically approaches to the limiting value obtained by the 2-D CFD simulation corresponding to a particular Gr_s .

The role of Θ , in determining the value of the Nusselt number, is described in Section VB. Table IV shows that for a particular ϕ , the Nusselt number varies with a change in Θ . On the other hand, Equation (33) signifies that for a particular Θ , the Nusselt number may vary with a change in ϕ . Consider a situation when Θ and other operating conditions [i.e., $(T_w - T_\infty)$ and fluid properties] are fixed. Then Equation (35) shows that Gr^* is also fixed. Under such a situation, the effect of change in ϕ (on the value of the Nusselt number) is demonstrated below with an example calculation.

In this example calculation, Gr^* is taken as 12 500. Two representative planforms, viz., planform-1 and planform-2, are considered. For planform-1, ϕ equals 1, and for planform-2, ϕ tends to infinity. For planform-1, 3-D CFD simulations give the value of Nu^* as 3.65. For planform-2, the value of Nu^* is 3.91 given by similarity theory [Equations (23) and (24)], and the value is very close to the results of 2-D and 3-D CFD simulations. Hence, the value of Nu^* for planform-1 is different

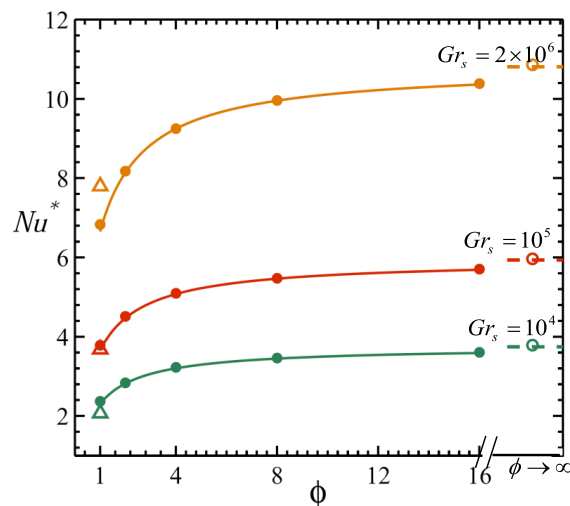


FIG. 12. Variation of Nu^* with aspect ratio ϕ at three Grashof numbers: comparison of present 3-D simulations, 2-D simulations, proposed correlation, similarity theory, and experimental values. Keys for colour: green [$Gr_s = 10^4$]; red [$Gr_s = 10^5$]; saffron [$Gr_s = 2 \times 10^6$]. Keys for line type and symbol: solid line [prediction of Equation (33)]; filled circle [3-D CFD simulations]; unfilled triangle [experimental correlation at $\phi = 1$]; unfilled circle [2-D CFD simulations]; dotted line [similarity theory] (all calculations correspond to the input parameters given in Table V).

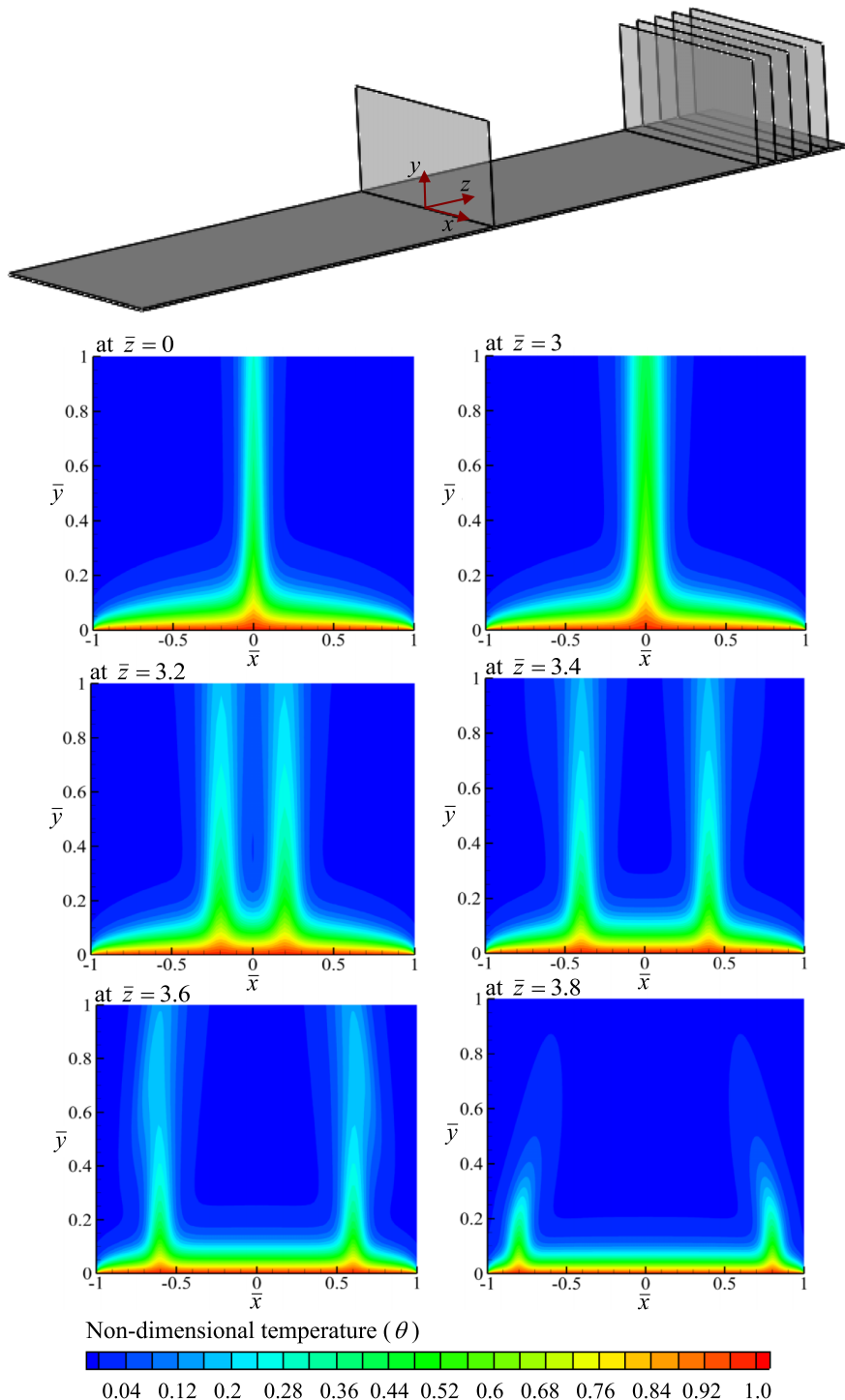


FIG. 13. Effects of physical corners and edges on the temperature distribution above a heated rectangular planform: prediction of 3-D CFD simulations (six representative slices are used to show the change in temperature distribution).

from Nu^* for planform-2, and this difference (7.1%) can be captured by the present theoretical correlation—since Equation (33) involves both geometric parameters, viz., Θ and ϕ .

On the other hand, as per our knowledge, not only the correlation provided by Fishenden and Saunders (Equation (36)) but all other previous empirical correlations for square and rectangular planforms consider only one geometric parameter, i.e., Θ . Thus, the existing empirical correlations

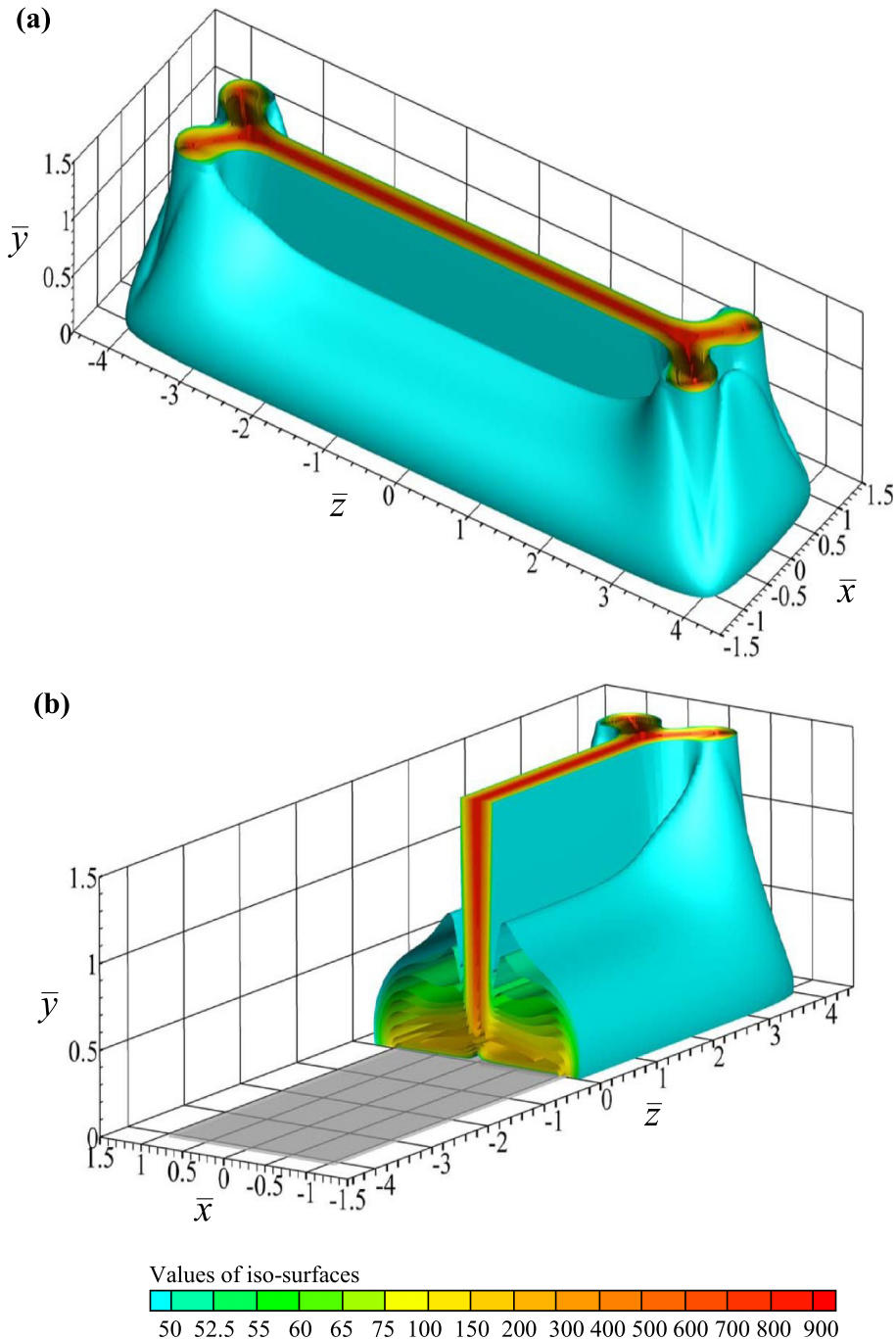


FIG. 14. Spatial distribution of non-dimensional velocity ($\sqrt{u^2+v^2+w^2}b/(2\nu)$) above a heated rectangular planform ($\phi = 4$): prediction of present 3-D CFD simulation. (a) Full view; (b) cut out view (cutting plane is at $z = 0$).

can be expressed in the general form,

$$Nu^* = C_{emp}(Gr^* Pr)^n, \quad (37)$$

where C_{emp} and n are two constants. For example, according to Lloyd and Moran,¹⁹ C_{emp} and n are, respectively, 0.54 and 0.25. Al-Arabi and El-Riedy²⁰ suggest that C_{emp} and n are, respectively, 0.5 and 0.25. For the example case (i.e., at $Gr^* = 12500$), various empirical values of Nu^* are 3.68 (according to the correlation of Fishenden and Saunders), 5.24 (according to the correlation of

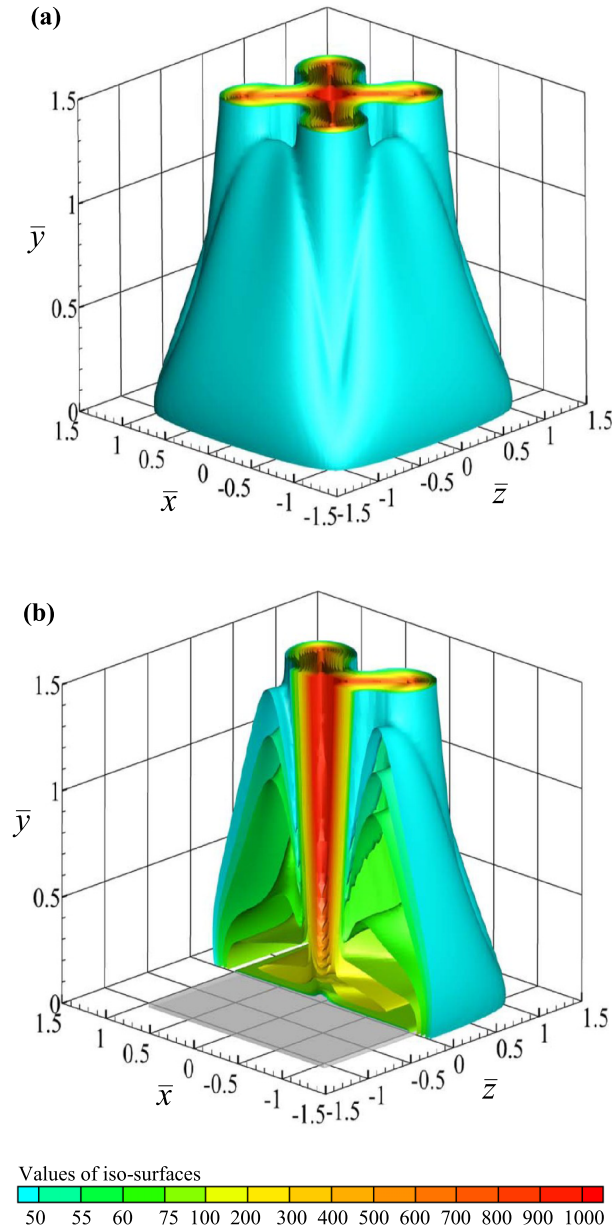


FIG. 15. Spatial distribution of non-dimensional velocity ($\sqrt{u^2 + v^2 + w^2}b/(2\nu)$) above a heated square planform: prediction of present 3-D CFD simulation. (a) Full view; (b) cut out view (cutting plane is at $z=0$).

Lloyd and Moran), and 4.85 (according to the correlation of Al-Arabi and El-Riedy). Moreover, the empirical correlations cannot differentiate between planforms of various ϕ .

E. Significance of physical corner in the planform

In Section V C, it is displayed that the distribution of surface heat flux on a heated square surface is different from the distribution of surface heat flux on a heated rectangular surface. In Section V D, it is shown that Nu^* for a square surface is markedly different from the Nu^* for a rectangular surface of large ϕ . These differences mainly evolve because of the presence of four physical corners in the planform. The effect of physical corners engulfs a large extent of a square surface, whereas it influences a comparatively smaller extent of a rectangular surface (Figure 11). The

impact of the presence of physical corners is not confined at the heated surfaces; it spreads in the three-dimensional space above heated surfaces. It is interesting to examine such three-dimensional distributions. This investigation is performed with the sample square and rectangular plates whose geometries are already described in Section V C. The operating conditions required for 3-D simulations are also kept the same as given in Section V C. Velocity distribution is studied for both surfaces, whereas temperature distribution is studied only for the rectangular surface.

Figure 13 shows the spatial distribution of temperature in the 3-D domain above the rectangular planform ($\phi = 4$). Six representative slices ($x - y$ planes) are shown at $\bar{z} = 0$, $\bar{z} = 3$, $\bar{z} = 3.2$, $\bar{z} = 3.4$, $\bar{z} = 3.6$, and $\bar{z} = 3.8$ above the heated surface. No striking difference in the temperature-distribution is found between $\bar{z} = 0$ and $\bar{z} = 3$, and the slice at $\bar{z} = 0$ is almost similar to the slice at $\bar{z} = 3$ (the only difference between these two slices is that the thickness of rising plume at $\bar{z} = 3$ is greater than that at $\bar{z} = 0$). Furthermore, these two slices are qualitatively similar to the contours obtained by 2-D simulations (Figure 4(b)) in which the effect of corners is totally absent. However, for $|\bar{z}| > 3$, the role of physical corners is reflected in the slice plot. With a progressive increase in \bar{z} (see the slices at $\bar{z} = 3$, $\bar{z} = 3.2$, $\bar{z} = 3.4$, $\bar{z} = 3.6$, and $\bar{z} = 3.8$), the following sequential observations can be made. At first, one billowing structure at $\bar{z} = 3$ divides into two billowing structures at $\bar{z} = 3.2$. Then, the distance between these two billows increases. Finally, the heated air rising from the hot surface cannot transport to a higher \bar{y} resulting into the decay of the height of the billowing structures. Additional physical feature to note in all six slices is that at all \bar{z} , temperature distribution is affected due to the edge-effect.

From Figure 13, the three-dimensional structure of the natural convective flow (including the rising plume) above the heated rectangular surface can be conceptualized. For representing the three-dimensional structure pictorially, further post-processing is performed. Figure 14(a) shows the full view of a composite structure which is composed by a number of iso-surfaces of non-dimensional velocity ($\sqrt{u^2 + v^2 + w^2}b/(2v)$). The values of iso-surfaces are mentioned in the figure caption. The flow situation near each physical corner constructs a rising column. Thus, near the end of each short side of the rectangular surface, effectively two rising columns are created. On the other hand, the flow situation near the middle of the rectangular surface (near $\bar{z} = 0$) results into a single rising column. The presence of corners does not affect the column near $\bar{z} = 0$. Figure 14(b) shows a cut out view obtained by a cutting plane which passes through $\bar{z} = 0$. The spatial distributions of velocity at (x, y) plane, which are not visible in the full view, can be observed in the cut out view.

Figures 15(a) and 15(b) show, respectively, the full view and a cut out view of the three-dimensional structure of the natural convective flow above the heated square surface. For the square surface, the effect of corners affects the velocity-distributions even near $\bar{z} = 0$. Thus the region, where a single rising column exists, is small. The top view of Figure 15(a) is, therefore, very different from the top view of Figure 14(a). The top view indicates the region through which the accrued fluid due to natural convective flow is transported into the ambient above heated surfaces. In summary, for the present flow configurations, the three-dimensionality of velocity and temperature fields chiefly arises due to the presence of physical corners.

VI. CONCLUSION

A rigorous and systematic computational study for the laminar natural convective flow above rectangular horizontal surfaces of various aspect ratios ϕ (from 1 to ∞) is presented. Two-dimensional CFD simulations (for $\phi \rightarrow \infty$) and three-dimensional CFD simulations (for $1 \leq \phi < \infty$) are performed to establish and elucidate the role of finiteness of the horizontal planform on the thermo-fluid-dynamics of natural convection. The results of the CFD simulations are compared with experimental data and similarity theory to understand how the existing simplified results fit, in the appropriate limiting cases, with the complex three-dimensional solutions revealed here.

It is shown here that although both similarity theory and 2-D CFD simulations represent a case of $\phi \rightarrow \infty$, there exists important differences between the prediction of 2-D CFD simulations and the prediction of similarity theory. The difference is arising because of two facts. Similarity

theory considers the plate to be semi-infinite (a plate with only a single leading edge). Hence, the 2-D CFD solution near the centre of the heated line, where a plume is formed, does not agree with the similarity solution (Figure 5). Secondly, the similarity theory is based on boundary layer approximation. Therefore, the solution near the leading edge of the heated line is not captured by the similarity solution (Figure 5). The region, which is far from both the leading edge and the centre, approaches toward similarity with an increase in the Grashof number (Figure 6).

Although the details of the results of 2-D CFD simulations may not match with that of the prediction of similarity theory, both methods give nearly identical values of the Nusselt number. This is so because the Nusselt number is the area-averaged non-dimensional surface heat flux. The averaged surface heat flux near the edges is greater than the boundary-layer-regions, whereas the averaged surface heat flux near the centre is less than the boundary-layer-regions (Figure 11). The integrated effect is such that the Nusselt number of the 2-D CFD solution is close to the Nusselt number of the similarity solution. This finding is true over a wide range of Grashof number (Figure 12).

The 3-D CFD simulations of the present paper are coordinated to clearly reveal the separate and combined effects of three important aspects of finiteness: the presence of leading edges, the presence of a planform centre and the presence of physical corners in the planform. It is to be noted that the finiteness due to the presence of physical corners in the planform arises only for a finite value of ϕ in the case of 3-D CFD simulations (and not in 2-D CFD simulations or similarity theory). The presence of physical corners leads to the following significant thermo-fluid-dynamic features. (a) Figure 11 shows that the distribution of surface heat flux on a heated surface alters with a change in ϕ (when the other operating conditions, including temperature of isothermal-surfaces, are kept fixed). For $\phi = 1$ (a square surface), the central part of the low- \bar{q}_w -zone is small and limbs are large. On the other hand, for $\phi = 4$ (a rectangular surface), the central part of the low- \bar{q}_w -zone is large and limbs are small. (b) Figure 13, which represents the temperature distribution above a heated rectangular surface, captures the transition from one billow to two billows. (c) Figures 14 and 15 show, respectively, a composite structure of a 3-D velocity field above a rectangular surface and that above a square surface. The top views of these two structures are different.

From Figures 8 and 9, the regions above a heated square surface, where in-plane velocity converts into out-of-plane velocity, can be identified. A comparison of Figures 8 and 9 reveals that, in general, the in-plane velocity is low in regions where the out-of-plane velocity is high. Another important feature of the flow field is that the magnitude of maximum out-of-plane velocity is much greater than the maximum in-plane velocity.

The present study demonstrates an important role of Θ (ratio of surface area to surface perimeter). Two sets of 3-D simulations are carried out when ϕ is varied from 1 to 16. Both sets contain a common geometry corresponding to $\phi = 1$. In the first set, ϕ is varied by fixing the length of the short side (b). In the second set, ϕ is varied by fixing the surface area. With an increase in ϕ , the Nusselt number obtained by the first set decreases, whereas the Nusselt number obtained by the second set increases (Table IV). However, for both sets, it is shown in Table IV that the Nusselt number decreases with an increase in Θ . Two limiting values of Θ corresponding to $\phi = 1$ and $\phi \rightarrow \infty$ are, respectively, $b/4$ and $b/2$.

A generic theoretical correlation for the Nusselt number (Equation (33)) is deduced for predicting the averaged surface heat flux for various rectangular surfaces (whose aspect ratio varies from 1 to ∞) over a wide range of Grashof number. The present paper establishes for the first time that two separate geometric parameters Θ (ratio of surface area to perimeter) and ϕ (aspect ratio) are simultaneously required to understand and fully quantify the effects of finiteness on the flow physics and heat transfer mechanisms of natural convection on horizontal surfaces. The validity of the new theoretical correlation is assessed in Figure 12 by comparing its prediction with an experimental correlation at $\phi = 1$, with similarity theory and 2-D CFD solutions at $\phi \rightarrow \infty$, and with 3-D CFD solutions in the range of $1 \leq \phi \leq 16$. The practical utility of the proposed correlation in predicting natural convective heat transfer rate from finite plates complements the physical understanding offered here on the effects of finiteness on the three-dimensional fluid dynamics.

¹ L. C. Burmeister, *Convective Heat Transfer* (John Wiley & Sons, New York, USA, 1983).

² J. P. Holman, *Heat Transfer (in SI Units)*, 9th ed. (Tata McGraw-Hill, New Delhi, India, 2008).

- ³ H. Schlichting and K. Gersten, *Boundary-Layer Theory* (Springer, New Delhi, India, 2004).
- ⁴ J. S. Turner, *Buoyancy Effects in Fluids* (Cambridge University Press, Cambridge, UK, 1979).
- ⁵ O. Shishkina and C. Wagner, "Modelling the influence of wall roughness on heat transfer in thermal convection," *J. Fluid Mech.* **686**, 568–582 (2011).
- ⁶ S. Samanta and A. Guha, "A similarity theory for natural convection from a horizontal plate for prescribed heat flux or wall temperature," *Int. J. Heat Mass Transfer* **55**(13), 3857–3868 (2012).
- ⁷ J. P. Mellado, "Direct numerical simulation of free convection over a heated plate," *J. Fluid Mech.* **712**, 418–450 (2012).
- ⁸ H. Shahmohamadi, "Analytic study on non-Newtonian natural convection boundary layer flow with variable wall temperature on a horizontal plate," *Meccanica* **47**(6), 1313–1323 (2012).
- ⁹ A. Vouros and T. Panidis, "Statistical analysis of turbulent thermal free convection over a horizontal heated plate in an open top cavity," *Exp. Therm. Fluid Sci.* **36**, 44–55 (2012).
- ¹⁰ A. Aziz, W. A. Khan, and I. Pop, "Free convection boundary layer flow past a horizontal flat plate embedded in porous medium filled by nanofluid containing gyrotactic microorganisms," *Int. J. Therm. Sci.* **56**, 48–57 (2012).
- ¹¹ A. Shapiro and E. Fedorovich, "Similarity models for unsteady free convection flows along a differentially cooled horizontal surface," *J. Fluid Mech.* **736**, 444–463 (2013).
- ¹² S. Saravanan and C. Sivaraj, "Coupled thermal radiation and natural convection heat transfer in a cavity with a heated plate inside," *Int. J. Heat Fluid Flow* **40**, 54–64 (2013).
- ¹³ S. Siddiqa, M. A. Hossain, and S. C. Saha, "The effect of thermal radiation on the natural convection boundary layer flow over a wavy horizontal surface," *Int. J. Therm. Sci.* **84**, 143–150 (2014).
- ¹⁴ K. Stewartson, "On the free convection from a horizontal plate," *Z. Angew. Math. Phys.* **9**(3), 276–282 (1958).
- ¹⁵ W. N. Gill, D. W. Zeh, and E. Del Casal, "Free convection on a horizontal plate," *Z. Angew. Math. Phys.* **16**(4), 539–541 (1965).
- ¹⁶ Z. Rotem and L. Claassen, "Natural convection above unconfined horizontal surfaces," *J. Fluid Mech.* **38**(1), 173–192 (1969).
- ¹⁷ A. Guha and S. Samanta, "Closed-form analytical solutions for laminar natural convection on horizontal plates," *ASME J. Heat Transfer* **135**(10), 102501-1–102501-9 (2013).
- ¹⁸ M. Fishenden and O. A. Saunders, *An Introduction to Heat Transfer* (Oxford University Press, 1950).
- ¹⁹ J. R. Lloyd and W. R. Moran, "Natural convection adjacent to horizontal surface of various planforms," *J. Heat Transfer* **96**(4), 443–447 (1974).
- ²⁰ M. Al-Arabi and M. K. El-Riedy, "Natural convection heat transfer from isothermal horizontal plates of different shapes," *Int. J. Heat Mass Transfer* **19**(12), 1399–1404 (1976).
- ²¹ R. J. Goldstein and K. S. Lau, "Laminar natural convection from a horizontal plate and the influence of plate-edge extensions," *J. Fluid Mech.* **129**, 55–75 (1983).
- ²² K. Kitamura and F. Kimura, "Heat transfer and fluid flow of natural convection adjacent to upward-facing horizontal plates," *Int. J. Heat Mass Transfer* **38**(17), 3149–3159 (1995).
- ²³ R. B. Husar and E. M. Sparrow, "Patterns of free convection flow adjacent to horizontal heated surfaces," *Int. J. Heat Mass Transfer* **11**(7), 1206–1208 (1968).
- ²⁴ D. J. Baker, "A technique for the precise measurement of small fluid velocities," *J. Fluid Mech.* **26**(3), 573–575 (1966).
- ²⁵ B. Gebhart, "Effect of viscous dissipation in natural convection," *J. Fluid Mech.* **14**(2), 225–232 (1962).
- ²⁶ F. Incropera and D. DeWitt, *Fundamentals of Heat and Mass Transfer*, 5th ed. (John Wiley & Sons, New York, USA, 1996).
- ²⁷ P. E. Dimotakis, "The mixing transition in turbulent flows," *J. Fluid Mech.* **409**, 69–98 (2000).
- ²⁸ Fluent 6.3 User's Guide 2006 Fluent, Inc., Central Source Park, 10 Cavendish Court, Lebanon, NH 03766, USA.
- ²⁹ B. Gebhart, L. Pera, and A. W. Schorr, "Steady laminar natural convection plumes above a horizontal line heat source," *Int. J. Heat Mass Transfer* **13**(1), 161–171 (1970).
- ³⁰ T. Fujii, I. Morioka, and H. Uehara, "Buoyant plume above a horizontal line heat source," *Int. J. Heat Mass Transfer* **16**(4), 755–768 (1973).
- ³¹ S. Grossmann and D. Lohse, "Fluctuations in turbulent Rayleigh–Bénard convection: The role of plumes," *Phys. Fluids* **16**(12), 4462–4472 (2004).
- ³² G. S. Gunasegarane and B. A. Puthenveetil, "Dynamics of line plumes on horizontal surfaces in turbulent convection," *J. Fluid Mech.* **749**, 37–78 (2014).
- ³³ E. P. van der Poel, R. Verzicco, S. Grossmann, and D. Lohse, "Plume emission statistics in turbulent Rayleigh–Bénard convection," *J. Fluid Mech.* **772**, 5–15 (2015).
- ³⁴ R. J. Whittaker and J. R. Lister, "Steady axisymmetric creeping plumes above a planar boundary. Part 2. A distributed source," *J. Fluid Mech.* **567**, 379–397 (2006).
- ³⁵ R. J. Goldstein, E. M. Sparrow, and D. C. Jones, "Natural convection mass transfer adjacent to horizontal plates," *Int. J. Heat Mass Transfer* **16**(5), 1025–1035 (1973).